

MACROSCOPIC WAVE DYNAMICS OF
BRIGHT ATOMIC SOLITONS

A DISSERTATION
SUBMITTED TO THE DEPARTMENT OF APPLIED PHYSICS
AND THE COMMITTEE ON GRADUATE STUDIES
OF STANFORD UNIVERSITY
IN PARTIAL FULFILLMENT OF THE REQUIREMENTS
FOR THE DEGREE OF
DOCTOR OF PHILOSOPHY

Michael Minar
April 2012

Dedicated to my parents Jeff and Jean, my brother Nick, and my wife Vera. For all
their love and support.

Abstract

On demand generation of single bright atomic solitons has been demonstrated using ultracold ^7Li atoms. These mesoscopic quantum bound states occur in one dimensional systems where attractive forces between particles balances dispersive and diffractive effects. Remarkably, these complicated objects of $N \approx 100$ atoms behave as a single quasiparticle with large effective mass and lifetimes of more than 6 seconds. I present details on our method of single soliton production as well as experiments that probe the quantum nature of these objects: specifically, their preparation in a minimum uncertainty wave packet and experimental signatures indicating the creation of a massive non-local superposition state. In addition, I report on the extension of our methods to multi-soliton production, and present the results of collision experiments with two solitons created at distinct points in a magnetic waveguide. The collisional dynamics include momentum exchange between the two solitons that depends on their relative phase as well as soliton-soliton fusion after multiple collisions. This phenomenology cannot be described by the standard one-dimensional theories used in previous work with atomic soliton trains, and is of interest to future experiments involving solitons for nonlinear atom interferometry and the use of entangled solitons for quantum information.

A Bose-Einstein Condensate of ^7Li is manipulated for the production of novel quantum many-body states. These include a fragmented state of weakly interacting incoherent solitons, and a pure single bright atomic soliton. In both cases these states result from the weak attraction between Lithium atoms and cooling the particles in a particular magnetic or hybrid magneto-optical potential.

The fragmented state is robust under evaporation in a highly anisotropic potential, and while there are potential applications as a bright atomic source with short coherence length, these experiments leave our findings at the stage of observation and basic state description.

Production of a pure single bright atomic soliton is more readily interesting for device applications and is studied in greater detail. Considerations for stability and efficient production are elaborated, and an experimental phase diagram is explored. In addition, I report on the lifetime of these states extending into many seconds. Quantum mechanical behavior is observed by studying the momentum spread of a localized wave packet upon release from an optical trap, in accordance with the Heisenberg Uncertainty Principle.

Lastly, I report on the extension of our experiments to multi-soliton production. Specifically, collision experiments with two solitons created at distinct points in a magnetic waveguide, separated by tens of microns. Spatial overlap between bright solitary matter-waves is observed for the first time. Additionally, the collisional dynamics include momentum exchange between the two solitons that depends on their relative phase. Lastly, soliton-soliton fusion is observed after multiple collisions. This phenomenology cannot be described by the standard one-dimensional theories used in previous work with atomic soliton trains, and is of interest to future experiments involving solitons for nonlinear atom interferometry and the use of entangled solitons for quantum information.

Acknowledgements

I am deeply indebted to my advisor, Prof. Mark Kasevich, for his guidance, inspiration, and faith during the course of this work. Mark's expertise and knowledge have shepherded this project from humble beginnings to what are hopefully the first in a string of exciting experiments for the advancement of knowledge in our community. Furthermore, his boundless enthusiasm for the new, novel, and unknown has been downright inspiring, and helped to see me through the more trying times of my tenure at Stanford. His vision for our work in the larger context of science and society is also extremely rich and it has been rewarding to be a part of that for the last several years. Lastly, I must acknowledge his ability to attract many talented, kind, and motivated people with whom I have been lucky enough to work with here at Stanford.

Of those, I would like to acknowledge Nick Cizek, Patrick Medley, David Berryreisser, Mingchang Liu, and Olaf Mandel who have all collaborated with me on these experiments. Mingchang and Olaf helped to show me the ropes before handing over an apparatus with a long and storied history. Nick and I grew into ownership of that apparatus together, and learned much from each other. I will always value his physical intuition, diverse set of skills, and intellectual curiosity as qualities to strive for in a good experimentalist. During the latter stages of my work, I was fortunate to be paired with an excellent post-doc, Patrick Medley. Patrick's ability to quickly grasp the essential structure of any new problem and immediately add value is a wonderful gift. I am also thankful for his enthusiasm, dedication, and his wealth of knowledge in many areas practical and theoretical. I have also been lucky to work with a junior

graduate student who quickly embraced our scientific mission and has left me assured that the experiment will reside in good hands after I leave. David has provided meaningful contributions from his very first day and was a pleasure to work with.

I've been fortunate to work with and learn from many others in the Kasevich group. My time at Stanford would not have been as productive or nearly as fun without them. Thanks are owed to Catherine Kealhofer, Geert Vrijen, Seth Foreman, Igor Teper, Jason Hogan, Dave Johnson, Alex Sugarbaker, Susannah Dickerson, Sheng-Wey Chiow, Hui-Chun Chien, Grant Biederman, Ken Takase, Todd Gustavson, and Jeff Fixler.

Contents

Abstract	v
Acknowledgements	vii
1 Introduction: Many-Body Physics with BECs	1
1.1 The push towards BEC and beyond	1
1.2 The role of interactions	2
1.3 The case of attractive interactions	3
1.4 Macroscopic quantum states and this work	4
1.5 Organization of this thesis	6
2 Experimental Apparatus and Procedure	8
2.1 Apparatus	8
2.1.1 Vacuum Chamber	8
2.1.2 Main optics for distribution	9
2.1.3 Frequency lock	11
2.1.4 MOT beam routing and dark MOT stage	13
2.1.5 New laser system	17
2.1.6 State preparation for magnetic trapping	18
2.1.7 Imaging System	19
2.2 Electronics	19
2.2.1 Trapping coils	19
2.2.2 Control Software	21
2.2.3 Image analysis	24

2.3	Procedure	25
2.3.1	Magnetic trap characterization	25
2.4	TOF experiments and experimental signatures	26
2.4.1	Data analysis for TOF experiments	29
2.4.2	Results	30
2.4.3	Theory of fragmentation	35
2.4.4	conclusion to TOF experiments	36
3	Deterministic Single Soliton Production	37
3.1	The optical trap	37
3.2	Seeding condensation	42
3.3	Soliton TOF experiments	43
3.3.1	Propagation without dispersion	43
3.3.2	phase diagram of soliton production	44
3.4	Conclusion	47
4	Macroscopic dynamics with bright solitons	48
4.1	Experimental procedure	49
4.1.1	Setup and Procedure	49
4.1.2	Procedure for waveguide flattening	50
4.2	A macroscopic quantum single particle	51
4.3	Measuring wave packet expansion	55
4.3.1	Heisenberg limited wave packet expansion	55
4.3.2	Questions of Adiabaticity	57
4.3.3	Stronger initial confinement	58
4.4	A potential interferometer or double slit experiment	59
5	Multiple Soliton Production and Experiments	60
5.1	Motivations for moving beyond previous work	61
5.2	Creating distinct solitons	61
5.3	Collision experiments: two solitons	62
5.3.1	Creation and initial collision	62

5.3.2	Phase dependent collisions	63
5.3.3	Soliton-soliton fusion	66
5.4	Conclusion	69
6	Conclusion	70
6.1	Future work	71
	Bibliography	74

List of Tables

List of Figures

2.1	Solid works figure of vacuum chamber	9
2.2	Lithium level structure diagram	10
2.3	Main optics layout	12
2.4	Spectroscopy optics layout	14
2.5	MOT beam routing	15
2.6	Photo of magneto-optical trap (MOT)	16
2.7	Efficacy of temporal dark MOT	17
2.8	Imaging System	20
2.9	Sequence of atom clouds after RF evaporation	21
2.10	Control computer screen shot	23
2.11	Setting the magnetic trap minimum	27
2.12	Absorption images of clouds after RF evaporation into quantum degeneracy	28
2.13	Atom number vs temperature for evaporation in cigar shaped trap . .	31
2.14	PSD vs temperature for evaporation in cigar shaped trap	33
2.15	Interaction energy vs temperature	34
3.1	Diagram of imaging and optical trap setup	38
3.2	Screen capture of imaging control station during the first successful load of our optical trap.	39
3.3	Comparison of atoms loaded into ODT vs held with magnetic trap . .	40
3.4	Characterizing optical trap frequency through parametric heating . .	41
3.5	Creation of single bright atomic soliton	43
3.6	Experimental Setup figure	44

3.7	Propagation of solitons in 1D potential	45
3.8	Experimental phase diagram of soliton purity	46
4.1	Macroscopic dynamics experimental setup	50
4.2	Raw cloud shots of soliton jumps	53
4.3	GPE simulation of CM wave packet expansion	54
4.4	Histogram of 60ms expansion data	55
4.5	Measured center of mass expansion rates	56
4.6	GPE simulation of cloud expansion	58
5.1	Creation and initial collision of two solitons	63
5.2	Phase dependent soliton collisions	65
5.3	Raw cloud shots of soliton-soliton fusion	67
5.4	Lifetime measurements of two colliding solitons	68

Chapter 1

Introduction: Many-Body Physics with BECs

1.1 The push towards BEC and beyond

In 1975 Schawlow and Hänsch introduced the idea that light could be used to cool atoms [1]. This idea was a great advance for the field of laser spectroscopy as it would allow for measurements of atomic resonances and linewidths to an extremely high degree of precision. In some ways however, the proposal was even more revolutionary. It offered a distinct paradigm shift in the field of atomic-optics. For the first time, light would be used to control the motion, external energy scales, and densities of these particles, rather than simply probe their characteristics. Within the next decade, techniques were developed to cool these gases to sub mK temperatures as well as trap them with optical and magnetic fields, achieving densities of $\approx 10^{11}$ atoms/cm³ [2]. In the 1980s the idea of forced RF evaporation was developed, allowing the preferential ejection of only the hottest atoms from these trapped gases [3, 4]. In 1995, amidst much excitement, the first realization of Bose-Einstein condensates with dilute atomic vapors was achieved [5, 6, 7]. An effect predicted 70 years earlier [8, 9], this milestone was honored in 2001 with the Nobel Prize in Physics. These experiments represented a significant advancement in the production of cold atomic vapor sources. Brighter than ever before, with densities of $\approx 10^{14}$ atoms/cm³, the true value of this result

was the ability to place all atoms into a single quantum state.

Further experimental and theoretical investigations have developed a more complete picture of the mechanisms for Bose-Einstein condensation, as well as provided advances in the technical aspects of BEC production: more atoms, colder temperatures, new atomic species, and faster/more robust production [10]. These are interesting objects of study in their own right and have led to important advances in our understanding and production capabilities of BECs.

This corpus of work has provided researchers, present and future, with a source of atoms that macroscopically occupy a single quantum state; offering the possibility of controlled quantum many-body experiments in fields as disparate as atom interferometry, quantum information, non-linear quantum optics, and the burgeoning field of quantum simulation. The experiments presented in this thesis certainly owe their existence to the advances made with BECs decades earlier. They represent an improvement in our understanding of BEC formation with attractively interacting atoms, as well as a significant advancement in our ability to produce bright atomic solitons.

What follows is a brief survey of experiments relevant to bright atomic soliton production. The presentation is not a complete one, but should be broad enough to provide a larger context for the work presented in the main experiments of this thesis.

1.2 The role of interactions

The first prediction of Bose-Einstein condensation assumed no interaction between particles. The effect was described as an equilibrium distribution of atoms following certain statistics below a specific temperature. However, the technique responsible for lowering the atom cloud to sufficiently cold temperatures, forced RF evaporation, is dependent on particle collisions. Once the hottest atoms are ejected, the remaining atoms must thermalize before the process is repeated. Thus, for BEC with dilute atomic vapors, the interactions between atoms has always been essential for the dynamics leading to condensation.

Interactions affect the nature of the final BEC state as well. A description based

on the ideal Bose gas predicts an infinitely compressible and perfectly stable BEC, which we know to be unphysical. The first two groups to achieve BEC did so in systems with repulsively interacting particles. A perturbative theory developed by Bogoliubov can be used to describe these condensates, and provide a framework for understanding quantum compressibility, phonon excitations, and thermal/quantum depletion in repulsively interacting BECs [11]. A BEC with attractively interacting atoms was realized third, and it also displayed deviations from the ideal Bose gas picture. Chief among these was the issue of condensate collapse. This type of condensate can only exist for atom numbers below some critical value, N_c . Once this threshold is crossed the compressibility becomes negative and the condensate will collapse inward on itself.

The diversity in observed phenomenology and consequent importance of interactions has only increased in the years since BECs were first produced. What were first perhaps thought of as technical subtleties to be smoothed away in an attempt to normalize BEC behavior have now become full fledged research programs in their own right. Interactions of both the repulsive and attractive variety are used as a driver in the formation of new and novel quantum many-body states. A few marquee examples include the use of repulsive interactions to trigger the superfluid to Mott transition in 2002 [12], spin-spin interactions used to generate entangled states for atom interferometry [13], and the production of atomic solitons in both repulsive and attractive systems [14, 15, 16, 17, 18]. It is this last line of experiments that this thesis work will contribute to.

1.3 The case of attractive interactions

Of the three landmark BEC experiments in 1995, the one with attractive interactions between atoms was completed third. This is in part due to the fragility of these states. Due to stability considerations, condensates with attractive interactions can only be formed below a critical atom number N_c . In the first successful experiment, the condensate contained only $N = 2 \times 10^4$ atoms and was smaller than the imaging resolution available. Evidence of condensation was inferred from diffraction pattern

produced by the imaging light on the detector.

The reason for this fragility can be understood by studying what has now become the canonical representation of an interacting BEC's wave function, the non-linear Schrödinger equation first used by Pitaevskii [19]. The negative internal energy from the BECs chemical potential must be weaker than the zero-point kinetic energy provided by the trapping potential used to hold the atoms. Else, the condensate will collapse under its own attractive forces [20, 21]. The critical atom number for stability depends on the particular trap geometry and the atom-atom coupling strength. A precise relation can be found by balancing the expectation value of these terms in the non-linear interacting Schrödinger equation. Due to these considerations, attractive BECs have slightly higher critical numbers in one-dimensional traps than in three dimensions.

The same scattering properties that make condensates challenging to form, and difficult to observe after formation, can also lead to the production of a novel many-body state called a bright atomic soliton. A particular solution to the nonlinear Schrödinger equation in one dimensional systems, a soliton is an atomic cloud where the weak attraction between atoms is balanced by the dispersion and diffraction of a localized wave packet [22]. This state is the matter-wave analog to well known phenomena in nonlinear wave systems, ranging from water waves in canals to light propagating in non-linear optical fibers [23, 24]. Producing solitons in atomic systems offers new opportunities to study quantum effects in what is traditionally a semi-classical system, but their value extends well beyond this line of inquiry. Solitons are a matter-wave source that has high brightness, coherence between all atoms, and is stable in shape for long periods of time. This makes solitons an attractive tool for emerging cold atom sensor technology [25, 26], quantum information storage [27, 28], and testing the limits of entanglement and decoherence [29, 30].

1.4 Macroscopic quantum states and this work

What is perhaps most remarkable about bright solitons is the extent to which this macroscopic quantum state of tens to thousands of atoms behaves as a single coherent

particle of effective mass $m_{\text{sol}} = N \times m$, where N is the soliton occupation number and m is the mass of the individual atomic constituent. In fact, the success of the campaigns listed above depends on this fact. Experiments that probe the limits of this picture and what deviations are expected are essential to that success. The first realizations of bright solitons focused primarily on their production and the ability to propagate without dispersion, with some investigation given to collisional properties [15, 16, 17]. However, these efforts produced solitons with non-adiabatic protocols and lacked sufficient control over internal and external degrees of freedom to explore richer phenomenology [31, 32, 33, 34].

Experiments with solitons not only afford us the opportunity to sharpen our conceptual understanding of complex many-body systems and develop new tools for future technologies, but in a very real way represent the continuation of a long tradition in coherent atom optics: the demonstration of well understood single particle quantum effects in systems of ever growing complexity and size. These campaigns push the domain of quantum mechanics further into the classical realm every year. It was just over 20 years ago that the state of the art was teasing the wave nature out of single atoms [35, 36, 37, 38]. Today, experiments around the world have demonstrated or are on the verge of demonstrating: matter-wave interference between massive super particles such as Buckyballs and DNA molecules [39, 40], cooling microcantilevers, membranes, or vibrating microtoroids to their motional ground state [41, 42, 43], and production of non-local superposition states of massive objects in optical cavities [44, 45].

The work presented in this thesis falls directly inline with these larger trends and goals in cold atom physics. Presented here is a new method for single bright soliton production under direct RF evaporation. This is achieved by manipulation of the local trapping potential the cold atom clouds sees during the evaporation process. The new procedure avoids the non-adiabatic step utilized in previous work and allows for pure soliton production at a particular place in a magneto-optic waveguide. Additionally, this method of production is able to produce a soliton in a minimum uncertainty state with respect to spatial localization and momentum spread. The spread of soliton center of mass position after 60 ms 1D time-of-flight exhibits a broad gaussian

distribution that agrees well with this picture. Remarkably, the soliton position varies from experiment to experiment, but remains in a pure quantum mechanical state for each. From this it is inferred that a continuous superposition of bright soliton states is being projected by the measurement procedure in each experiment. This would be an elegant demonstration of quantum mechanics on a many particle scale. Lastly, collisional properties between solitons are studied when techniques presented in previous chapters are extended to produce two independent solitons at different points in a one-dimensional waveguide. The limit of the single coherent particle model is tested, and it is found that saturation and nonlinearities can have a substantial effect on system behavior. In contrast to previous work, the relative phase between solitons is not fixed at a particular value but allowed to vary randomly from shot to shot. This allows for the observation of phenomenology not contained in the 1D Gross-Pitaevskii theory, including: mass transfer between colliding solitons and soliton-soliton fusion. To my knowledge, it is the first time these effects have been observed in an atomic matter-wave system, though these effects are known to occur in systems with optical solitons.

1.5 Organization of this thesis

The rest of the thesis is divided into 5 chapters. Chapter 2 describes the experimental apparatus and procedures used to generate BECs and solitons with ultracold ^7Li . It also discusses preliminary results involving our attempt to produce these objects under direct evaporation in a highly anisotropic magnetic trap. These results are interesting insofar as they elucidate mechanisms which frustrate the formation of a pure soliton state in traps of this nature. Chapter 3 describes a new procedure for generating single bright solitons and studies its efficacy. In chapter 4, the experiment studying Heisenberg limited expansion of the soliton's center of mass wave packet is described. The object is prepared in a minimum uncertainty, leading to the production of a mesoscopic non-local superposition state; or atleast, so I infer. The final set of experiments are described in chapter 5, where a second optical trap is used to seed the production of an additional bright solitary wave. The collisional properties

of the two solitons are studied and a variety of novel behavior is observed, including: momentum transfer between solitons, atom radiation, and soliton-soliton fusion. Lastly, in chapter 6 some concluding remarks and future plans for the apparatus are recorded.

Chapter 2

Experimental Apparatus and Procedure

Experiments with cold atoms are comprised of a number of components which can generally fall into one of three categories: vacuum chamber, optics, and electronics. The construction of the system's vacuum chamber has been described previously [46], and so will only be discussed briefly. The first substantive part of this chapter will focus on the optical setup used to cool and detect ${}^7\text{Li}$ and the electronics for trapping the atoms as well as higher level experimental control and analysis of the data.

2.1 Apparatus

2.1.1 Vacuum Chamber

The vacuum chamber was constructed before my tenure on the experiment. Still, it is helpful to display a solid works mock up of the system while describing the flow of an experimental run. The chamber can be seen in Fig. 2.1. In brief, a sample of Lithium is heated to $\approx 630\text{K}$ where it becomes a vapor and enters the 2D region (6" cube). Transverse cooling beams are sent reflected through this region multiple times to collimate the atomic beam, which then is directed through a differential pumping stage and into the science chamber. A 3D MOT is created in this octagonal

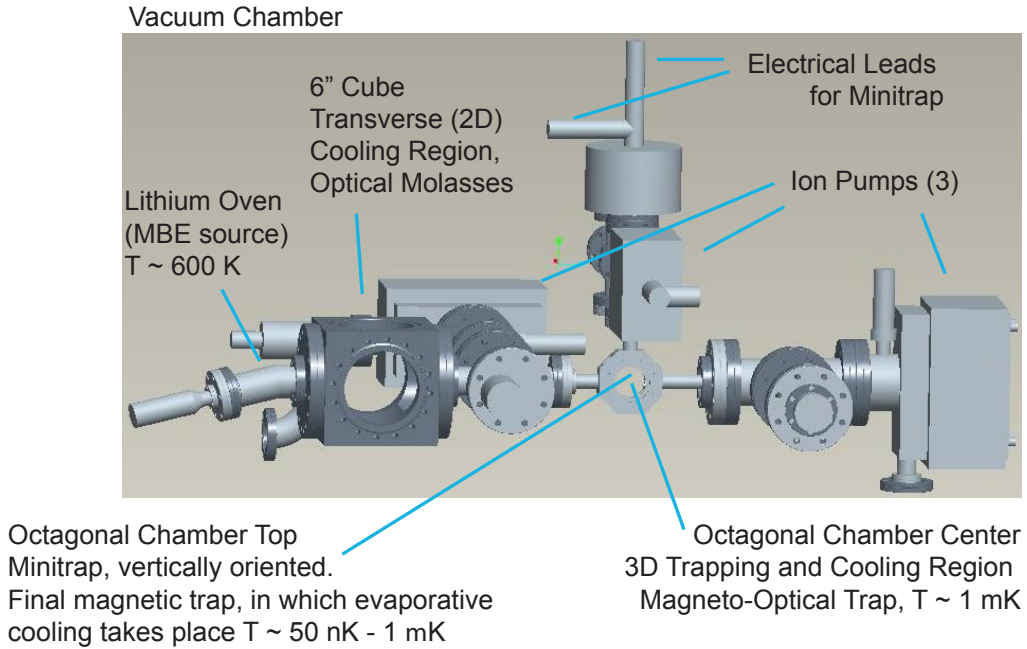


Figure 2.1: Annotated mock up of Lithium vacuum chamber. The various sections and pieces are labeled and milestones in the experimental sequence are called out.

shaped chamber where we load for 90 seconds. At that time, after approximately 1 billion Lithium atoms have been captured a final optical cooling stage takes place. Next the atoms are shuttled upwards to a custom Ioffe-Pritchard (IP) trap where RF evaporation is used to achieve quantum degeneracy and Bose-Einstein condensation.

2.1.2 Main optics for distribution

Both the D1 and D2 transitions of ${}^7\text{Li}$ are used in the experiments presented here, centered near 671 nm. The D2 transition is used for cooling, repump, and imaging of our atoms, while the D1 is used for hyperfine level state preparation. A figure of the level structure as well as energies associated with specific transitions is seen in Fig. 2.2. Some considerations relevant to cold atom experiments with Lithium can be seen immediately from this level structure. First, the splitting between the $F = 1$ and $F = 2$ ground states is only 800 MHz. This allows us to easily operate a MOT in

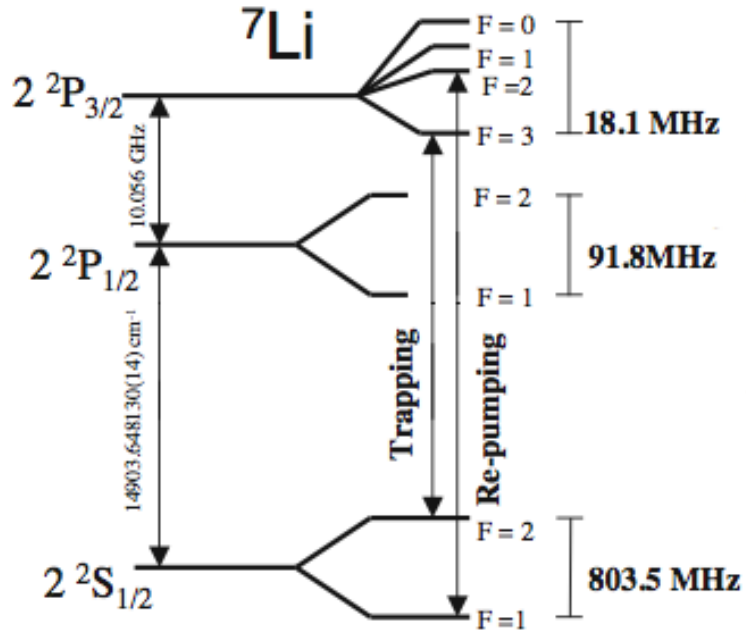


Figure 2.2: Level structure of ${}^7\text{Li}$. Trapping and repump transitions are shown explicitly. State prep occurs on the D1 line between $F = 2$ and $F' = 2$. Lastly, imaging light utilizes the same transition as cooling, but without any red detuning.

the $F = 2$ ground state without fear of spin flipping collisions leading to atom loss. This is in contrast to Rubidium and Cesium where the splitting between ground state F levels is several GHz. Empirically, I have found that MOT beams with intensity of 20 mW/cm^2 and a few MHz detuning provide sufficient depth to recapture atoms which have undergone these collisions. Second, one can see that the excited hyperfine levels in the $F' = 2$ and $F' = 3$ states overlap. This makes sub doppler cooling impossible with Lithium. Even more importantly, it leads to fast depopulation of the $F = 2$ state and the need for repumping beams of reasonably strong intensities. These considerations inform the experimental setup.

Of additional note is the high power nature of Lithium cold atom experiments. The material has a high melting point amongst the alkalis, 181 C , and we must heat our samples to over 300 C to achieve suitable vapor pressures inside the 2D chamber.

This combined with the small mass of Lithium leads to high probable and average velocities for atoms in the gas. To account for the large changes in velocity for capture and cooling, a Zeeman slower is often used to compensate for large doppler shifts of the atom's resonance as it is slowed from 1500 m/s to 1 m/s. However, these structures are often large and cumbersome and are not used in this apparatus. Instead, the MOT beams are spectrally broadened by 150 MHz to ensure the resonant interaction between light field and atom over the course of deceleration and trapping. As a result, nearly 700 mW of power at 671 nm is required for the MOT beams and 2D cooling light.

Historically these high powers were achieved by operation of a 899 coherent dye laser. A significant improvement to the optics setup was to replace the dye laser with a solid state system, consisting of a coherent vortex as master and two Sacher tapered amplifiers as slaves. The main optics layout for light amplification and distribution is diagramed in Fig. 2.3. The MOT (or comb) beam is too high power to be fiber coupled and are directed towards the atoms through free space.

It is worth noting that the repump sideband is added to the MOT beam at the first electro-optic modulator (E1 in Fig. 2.3) and spectral broadening is accomplished by overdriving the second electro-optic modulator (E2 in Fig. 2.3) before the light is sent through the second tapered amplifier. This sub GHz modulation is well within the bandwidth of the Sacher TAs, and thus the frequency profile of the MOT beam is boosted without distortion. AOMs A1 and A2 are used to pick off light from the main beam path and shuttle it the cooling, repump, and imaging fibers. These elements allow for fast analog control of beam amplitude. The fiber coupled beams' detunings are controlled by A3 and A4. The final cooling and repump light for the compressed MOT stage are combined on a cube (C3) and then aligned to the same fiber. This ensures good alignment onto the MOT once the light is directed from the fiber.

2.1.3 Frequency lock

Modulation transfer spectroscopy is used to lock the lasers to their appropriate lines. The main laser used for cooling, repump, and imaqing light is locked to the

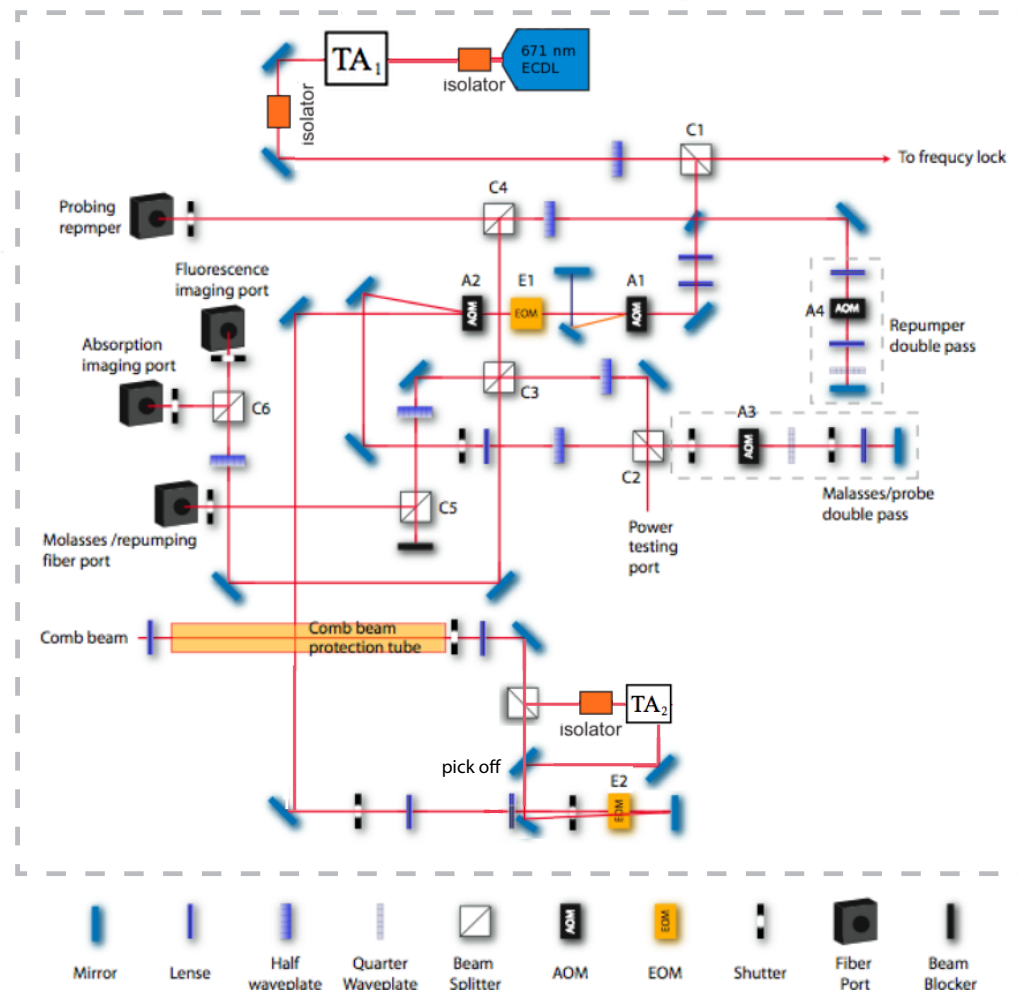


Figure 2.3: Optics layout of laser system and power distribution.

$|F, m_f\rangle = |2, 2\rangle$ to $|F', m'_f\rangle = |3', 3'\rangle$, while an additional laser used for hyperfine state preparation is locked to the $|2, 2\rangle$ to $|2', 2'\rangle$ D1 line. This is a variant of doppler free saturation spectroscopy where the saturation beam is amplitude modulated via a Lock-in detector. The probe beam is then detected at this frequency with a photodiode, and modulations in detected power due to the saturation beam's time variance are seen. This technique allows for regular spectroscopy techniques to be moved from DC to a particular frequency band, in this case 40 kHz.

A particular technique that is useful for our experiment is to frequency detune the saturation beam by ~ 150 MHz to the blue of the Lithium resonance. As stated above Lithium must be heated to a high temperature in order to evaporate sufficient numbers of atoms for spectroscopic purposes. The likelihood of finding atoms at velocities near $v = 0$ is thus very low. By shifting the relative frequency of the saturation beam with respect to the probe beam the locking scheme will address atoms moving at approximately 50 m/s towards the probe beam. The ratio of atoms in a particular window of velocity follows a Maxwell Boltzmann distribution at these temperatures. For a Lithium gas at 300 C the number of atoms in a 1 m/s window centered around $v = 50$ m/s is more than 7 times the number in a similar window centered around $v = 0$ m/s. A diagram of the spectroscopy/lock setup for the main laser can be seen in Fig. 2.4.

2.1.4 MOT beam routing and dark MOT stage

The vacuum chamber is enclosed by a black cardboard box so as to guard against stray light during RF evaporation. Beams are routed into this box via the comb beam tube or the fiber ports in Fig. 2.3. Once inside, the comb MOT beams are split four ways, displayed in Fig. 2.5. Due to polarization constraints the light from the 1st TA is sent to the two diagonal beams and light from the 2nd TA is split between the horizontal MOT beam and the 2D molasses light. Power balance is important for a good MOT load. The alignment procedure involves equally splitting light from the 1st TA between the two 45 degree beams, and using wave plate W3 to balance peel off an equal amount of power from the 2nd TA's beam. The remaining light is sent

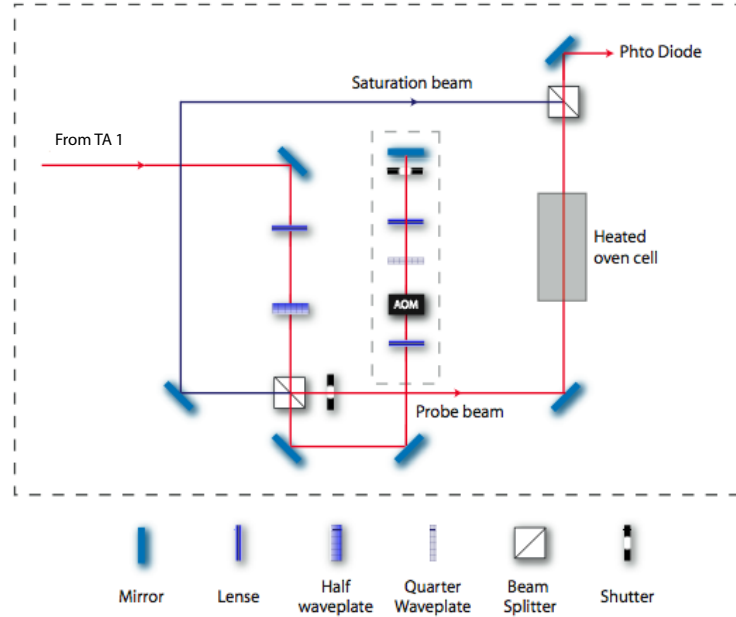


Figure 2.4: Optics layout of laser system and power distribution.

to the 2D stage where it is used to cool the transverse velocity of atoms flying away from the oven region.

After the MOT is loaded for 90 seconds the comb beams are switched off and a final temporal dark MOT stage begins. Light exiting from the "molasses/repumper" fiber port is used. These beams are aligned coincident with the comb MOT beams and function in a similar fashion, but with two differences. First, there is only a single frequency cooling frequency and a single repump frequency used, both of which are detuned roughly $\Gamma/2$ to the red of their respective transitions, where $\Gamma/2$ is the natural linewidth of the $F = 3$ state. Second, the intensity of repump light is dropped to approximately 1/10 of saturation to initiate a temporal dark MOT for the final stage of optical cooling. A picture of a full MOT at the end of our load stage and just before the temporal dark stage can be seen in Fig. 2.6. This picture was taken with a commercial digital camera. The MOT contains approximately 1 billion atoms.

The idea in this last step is to achieve the highest possible initial phase space density before transferring the atoms to our magnetic trap. Normally, the density

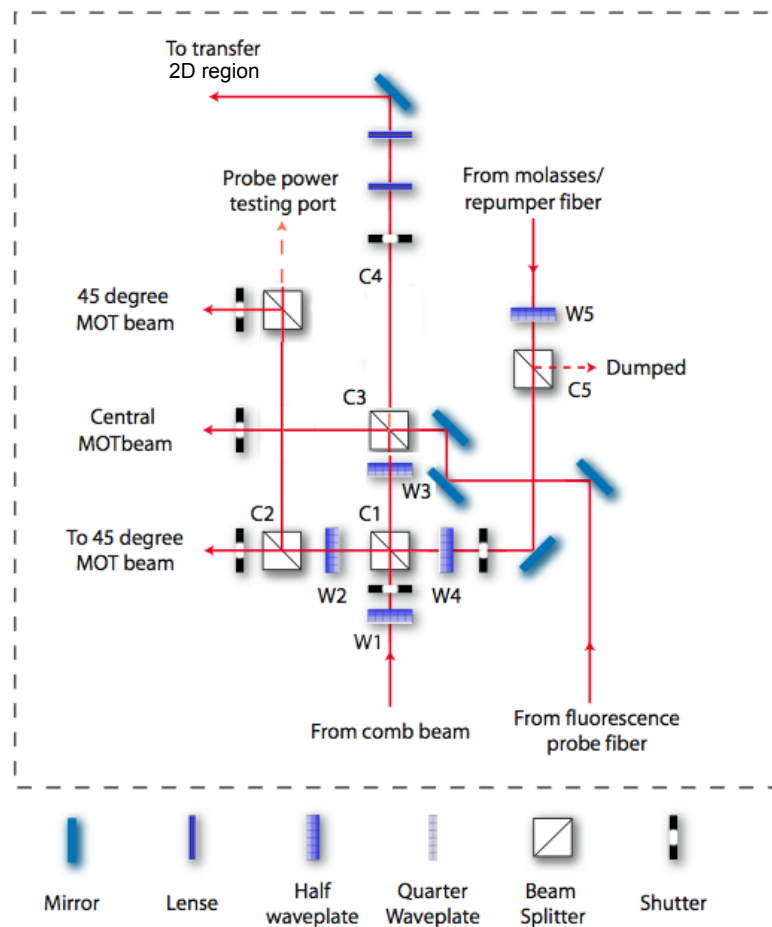


Figure 2.5: Distribution of light for MOT beams and dark MOT beams.

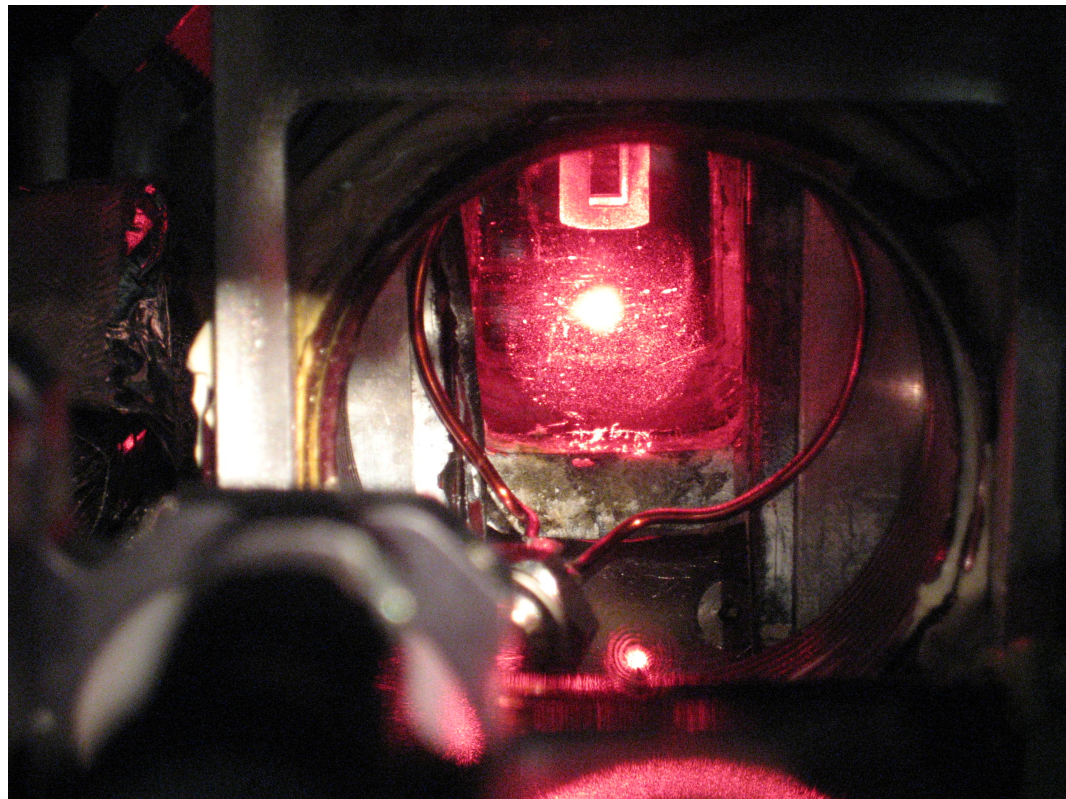


Figure 2.6: Lithium MOT loaded for 120 seconds. The imaging optics have been removed for clear line of sight to the atom cloud. The MOT contains $\approx 10^9$ atoms. The RF evaporation coil can be seen in the foreground directly in front of the vacuum chamber window and inside one of the MOT coils. Directly above the MOT atoms is the custom Ioffe-Pritchard trap (minitrap).

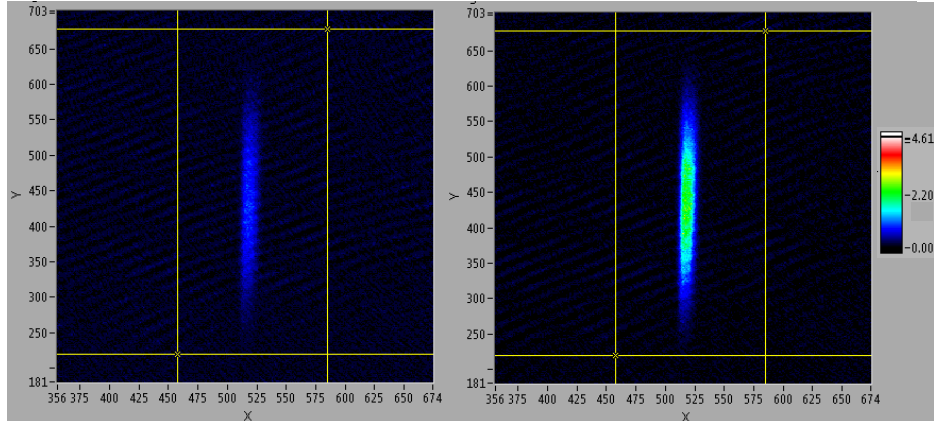


Figure 2.7: Absorption images for atoms in IP trap evaporated to 1 MHz above trap bottom. Panel on left does not utilize temporal dark MOT before transfer to magnetic trap, causing evaporation to begin with a lower initial phase space density.

of a MOT is limited by two factors: re-radiation pressure and attenuation of the MOT beams in optically thick clouds. The temporal dark MOT mitigates both of these effects by drastically reducing the repumper intensity for a brief period of time. This causes atoms to spend the majority of their time in the $F = 1$, or dark, state. The cloud becomes optically thin and trapping forces near the cloud center are restored, leading to an increase in density. In addition, the cloud becomes optically thin to reradiated light from cooled atoms. The probability that a neighboring atom will be susceptible to heating from reradiated light drops significantly during this process as well. This method was first demonstrated in Sodium MOTs at MIT in the early 90s [47], but the technique is applicable to Lithium systems as well. The improvement in this experiment can be seen in Fig. 2.7 where absorption images of atoms transferred from MOT to Ioffe-Pritchard trap are shown. The difference in final MOT phase space density leads to a factor of 2.75 in atom number after transfer.

2.1.5 New laser system

A significant advance in stability of the experiment was made when the old dye laser system was replaced with an all solid state solution. Previously, a Coherent 899 dye

laser pumped by an Inova Argon Ion laser was the only way to generate sufficient power at 671 nm. However, recent advances in laser diode technology has eliminated this constraint. Utilizing a New Focus Vortex II laser system as a master and two Sacher tapered amplifiers for power boosting.

The composite system is quite stable. The master is used to inject the first TA with approximately 10 mW of light. Polarization as well as mode matching of seed to TA output are important for maximum efficiency, but this is readily achieved with a half wave plate and long focal length lens. The output of this amplifier is routed for spectroscopy as well as MOT and imaging beams with a portion being picked off and sent through a fiber to seed the second tapered amplifier. The fiber acts as a spatial filter and adds stability to the second seed beam. 10 mW is used for seeding this tapered amplifier as well. This is diagramed in Fig. 2.3.

2.1.6 State preparation for magnetic trapping

Upon completion of initial capture and cooling the atoms must be prepared in a particular magnetic sublevel for magnetic trapping. A second Vortex II laser centered on the D1 line is used to optically state prepare the Lithium atoms into a low field seeking hyperfine state. After the dark MOT stage, the atoms are released from their optical-magnetic trap and a strong bias field is turned on, so as to establish a well defined axis for spin precession. The light from the second Vortex is circularly polarized and directed along this quantization axis towards the atoms, before being retro reflected to shine on the atoms again. If the polarization of the light is pure, the absorption of a photon will shift the atom's m_f state by +1 and place it in the $F' = 2$ manifold. Spontaneous emission will then cause the atom to relax back to the $F = 1$ or $F = 2$ ground state with an average change of 0 to the m_f hyperfine level. If the atom falls to the $F = 1$ ground state, then repump light will quickly bring it back to the $F = 2$ manifold, also with no net change in m_f state on average. This process is repeated causing a net drift in the atom's hyperfine state until it arrives in the $|2, 2\rangle$ state, which is a dark state for this pumping scheme. Once here, the atoms no longer scatter any photons and will remain unperturbed so long as the bias magnetic field

preserves its spin polarization.

This stage of the experimental procedure should be completed as quickly as possible, as the atoms are necessarily not trapped during this step, resulting in a loss of phase space. With careful alignment of the bias magnetic field and high fidelity of the state preparation light's polarization to right circular, I was able to accomplish near complete optical pumping in $300 \mu\text{s}$. This is inferred from a decay in the measured fluorescence of the atom cloud as more and more atoms are pumped into the dark state. The efficiency of this step is further noted in the capture rates of our Ioffe-Pritchard (IP) trap, where the use of this process increased the initial number of atoms by a factor of 2.

2.1.7 Imaging System

At the conclusion of evaporation clouds are prepared for imaging. This is done by shining resonant absorption light onto the atoms and projecting the shadow onto a CCD camera. The imaging system is a simple telescope with 75 mm objective and 200 mm imaging lenses. The particular camera used is an ANDOR Ixon3 888, with a $13 \times 13 \mu\text{m}$ pixel size, yielding a final imaging resolution of 5 microns. The atoms are imaged with $\sigma+$ light to maximize the resonant cross section and attempt access a cycling transition between the $|2, 2\rangle$ and $|3', 3'\rangle$ states. However, shots taken in-situ do not lend themselves to this scheme because of the wandering of the magnetic field vector in trap. Consequently, the atoms can depump to the $F = 1$ manifold during the $10 \mu\text{s}$ imaging time. To compensate for this, repumping light is shone on the atoms from below. A schematic of the imaging system can be seen in Fig. 2.8

2.2 Electronics

2.2.1 Trapping coils

Various current carrying coils are used to trap the Lithium atoms at different points in the experimental cycle. In addition to the standard MOT coil and Ioffe-Pritchard trap coils which are well described in the literature, this experiment utilizes a magnetic

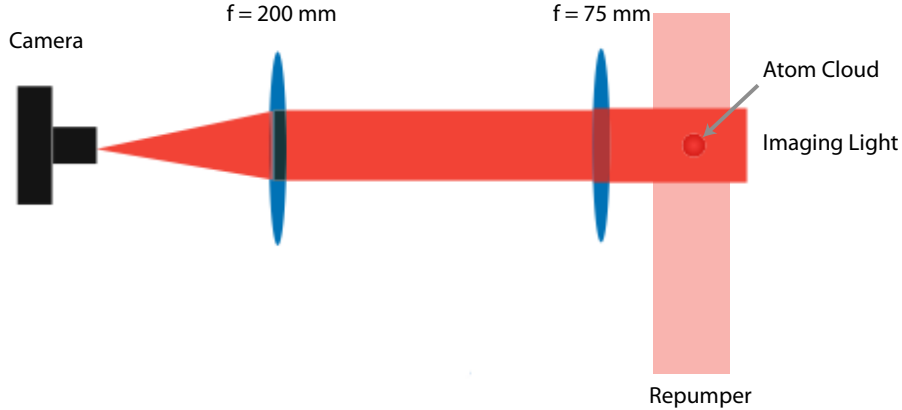


Figure 2.8: Absorption imaging with repumping

elevator to shuttle the atoms from MOT region to the IP trap. This procedure has been well documented in a previous thesis [46], but a few considerations are worth noting here.

The high power nature of Lithium experiments extends to the electronics side as well. The light mass of our atom combined with the ineffectiveness of sub-doppler cooling results in a temperature of $500 \mu\text{K}$ even after the use of the temporal dark MOT stage. Before transfer to a magnetic trap, the atoms must undergo optical state preparation. During this stage the atoms are not trapped and fly away at 0.8 m/s . The optical processes involved in state preparation can be accomplished in 100s of microseconds, but what is more damaging to our cause is the time required to turn on and off the currents needed for magnetic confinement. The MOT coils require only 10 A and can be switched off quickly without issue; however, the same coils are used to recapture the atoms after state preparation in a quadrupole trap and 50 A are required. A large capacitor of $1/2 \text{ F}$ is used to source enough current to achieve a 1 ms turn on time. Empirically, we find that anything longer than this results in a sharp drop in phase space that would lead to inefficient evaporation later.

Once recaptured by the quadrupole trap, the atoms are shuttled vertically upward by approximately 2 cm to sit inside the IP trap used for evaporation. This trap is millimeter scale and is housed inside the vacuum chamber. As a result it only requires

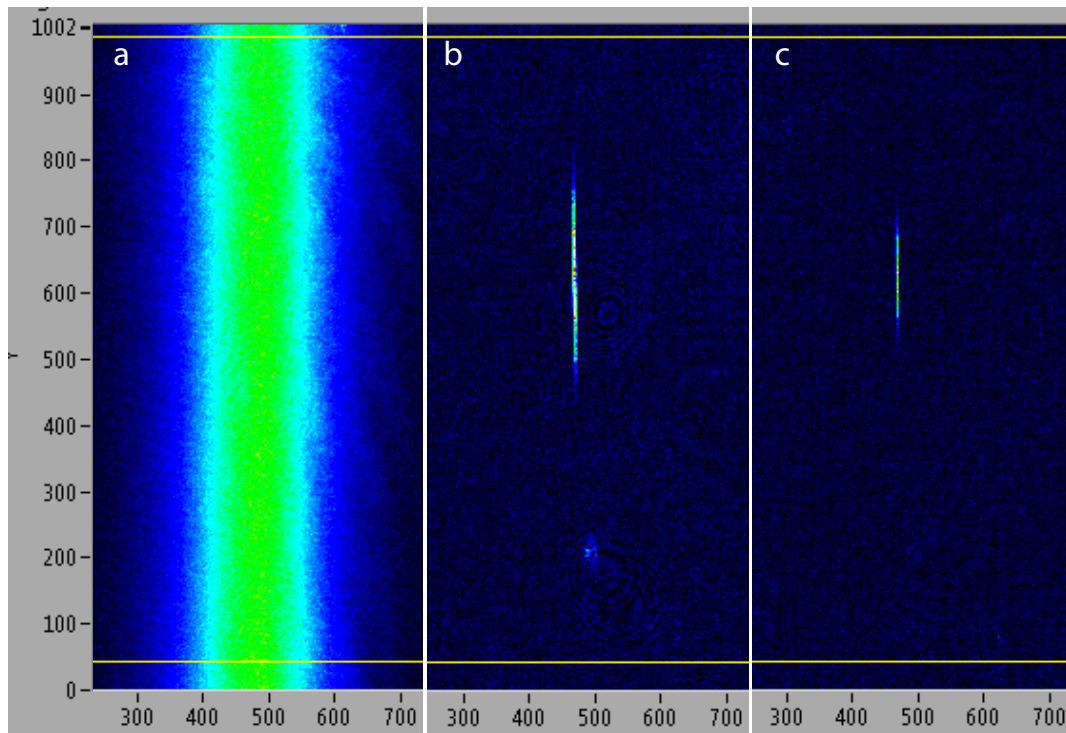


Figure 2.9: Absorption images for atoms in IP trap with no evaporation (**a**), evaporation to 1 MHz above trap bottom (**b**) and evaporation to 400 kHz above trap bottom (**c**)

a single loop and dissipates only a few Watts of power, yet is still able to achieve tight confinement in two of three dimensions. The trap is cigar like with an aspect ratio of 70:1. Efforts to achieve a quantum degenerate gas with Bosonic Lithium in this trap have been described previously [48]. A sequence of example shots showing the atom cloud initially and near the end of evaporation is shown in Fig. 2.9.

2.2.2 Control Software

Modern day AMO experiments require precise timing control over a long experimental sequence. Voltages and current ramps must be triggered with microsecond resolution over the course of a run that can last for multiple minutes. To achieve the level of precision required, a Field Programmable Gate Array (FPGA) is used to set the

timing sequence. These chips combine the precision and robustness of an application specified integrated circuit with the flexibility of reprogrammable hardware, thus allowing us to run different experimental sequences. For timing fidelity all that is required is a local reference clock, provided by either GPS or a quartz oscillator.

Matlab is used as the integrated programming environment, allowing the user to work mostly in a high level language. Matlab talks to the FPGA with the aid of helper functions written in HDL and initially coded by Olaf Mandel, a post-doctoral fellow on this project. The FPGA's output has been connected to a 40 channel analog out board from National Instruments. This nexus of timing circuitry, voltage outs, and a high level language interface constitutes the brain of this apparatus. A particular experimental sequence is inputted with a graphical user interface, constructed in matlab. Once created, this sequence can be saved and recalled at a later date. Each time the experimenter chooses to run a particular sequence the FPGA is reprogrammed with a new voltage-timing sequence, and runs (either once or continuously) until control is reasserted by the user interface program. A screen shot of the user interface can be seen in Fig. 2.10

The matlab environment allows for variables and lists of values to be assigned along with literals via the GUI. This offers a great opportunity for automation of the hardware via software. Lists encompassing hundreds of individual runs can be created with relative ease and these can be used to map out large regions of experimental phase space. Once suitable efforts had been undertaken to stabilize and dedrift the apparatus so that it could run for hours unattended, this boost to our control capabilities allowed for a variety of experiments to be run with full automation. The data presented in the later chapters would have been painful to collect without these features. Experimental runs would often take days to complete, after sufficient averaging and exploration of different parameter values was complete. As a final flourish, the matlab program was set to interface with twitter upon the completion of a long experimental run. This was convenient as it allowed the experimenter to check the status of the system from anywhere in the world simply by following tweets from LiSolitonMaker.

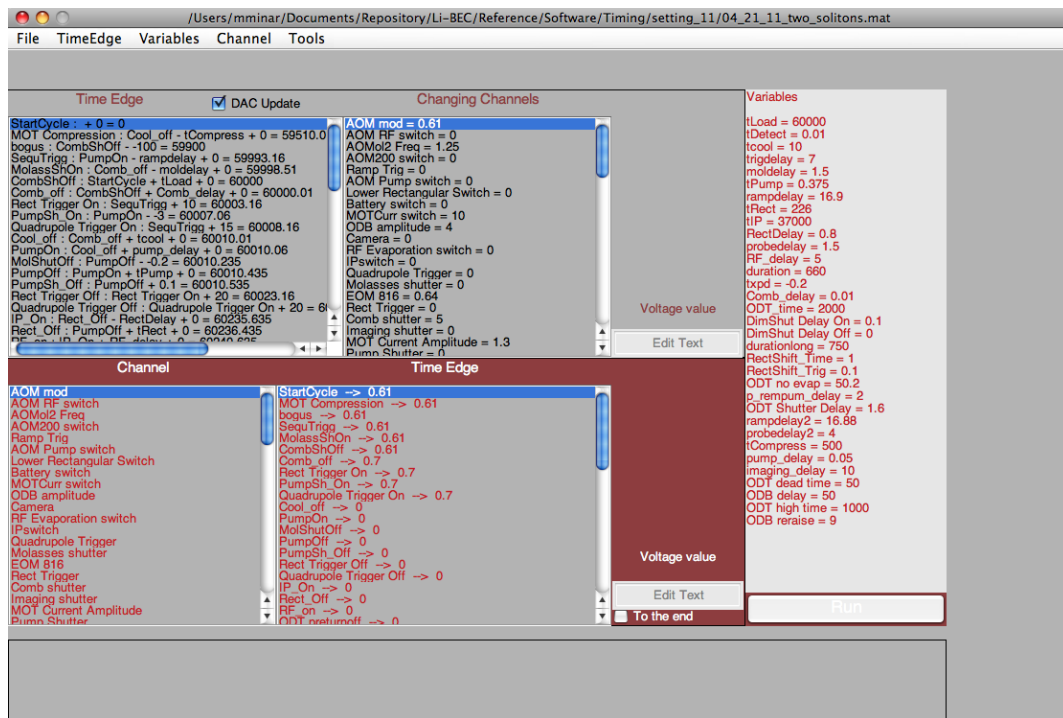


Figure 2.10: GUI used to construct experimental sequences in the Lithium apparatus

2.2.3 Image analysis

The optical component of the imaging system is described above. After the final stage of evaporative cooling and some amount of time of flight (TOF), three images are taken of the atoms. These three images are used to reconstruct the atomic density profile of the cloud at the time of the first image. Almost all of the experimental signatures are based on what the atom density profile is at the end of the experiment, and so it is essential that the signal is read out with high fidelity.

The first two images are taken with an exposure of $10 \mu\text{s}$ each, with and without atoms present respectively. The third and final frame is a measurement of the dark field, no light beams are on. Frame 3 is subtracted from frames 1 and 2, and then a measurement of optical attenuation from the atom cloud is constructed by dividing frame 1 by frame 2. The resultant image should register a 1 anywhere the light field was unobstructed and a value below 1 but still positive for pixels where the atoms appeared. A precise relation between measured signal and calculated atom number is:

$$OD_{\text{measure}} = -\ln \left(\frac{\text{Image}_{\text{Atoms}} - \text{Image}_{\text{dark}}}{\text{Image}_{\text{noAtoms}} - \text{Image}_{\text{dark}}} \right) \quad (2.1)$$

$$= \sigma \int n(x, y, z) dy \quad (2.2)$$

where

$$\sigma = C^2 \frac{\lambda^2}{2\pi} \left[1 + \left(\frac{\delta}{\gamma} \right)^2 \right] \quad (2.3)$$

The right hand side of eq. 2.2 is the integrated column density along the imaging axis (y axis), with $n(x, y, z)$ being the local atomic density at some point in space and σ being the light atom cross section. For $\sigma +$ resonant light, the equation 2.2.3 reduces to $\sigma = 0.7 \times \lambda^2 / (2\pi)$. The prefactor of 0.7 comes from an analysis of the steady state population of the ground hyperfine states for atoms bathed in light with experimental polarizations, detunings, and intensities, as well as strength of bias magnetic field for TOF experiments.

2.3 Procedure

The components of the apparatus described above as well as others are used in the experimental procedure to generate cold Lithium clouds in a cigar shaped trap. We begin by loading $N_a \approx 10^9$ atoms into a magneto-optical trap. A temporal dark MOT is used for a final cooling stage before the atoms are optically pumped into the $|F = 2, m_F = +2\rangle$ trap state, loaded into a magnetic quadrupole trap, and transported into a final cigar-shaped IP trap.

RF evaporation is done by mixing together a constant 780 MHz signal and a swept RF output from a Digital Data Synthesizer (DDS) board; then, sending this output through a 20 W amplifier and into an antenna placed near the atoms. This ramp is triggered by a voltage switch and runs from 950 MHz to some final RF cut which determines cloud temperature. The 0 magnetic field hyperfine splitting between trapped and anti-trapped states in ${}^7\text{Li}$ is $\nu_{\text{HFS}} = 803.534 \pm 0.077$ MHz [49], so the minimum RF transition must be larger than this for traps with non-zero minima. This value is set during calibration between 804.02 and 804.12 MHz. For RF cuts below 805 MHz the cloud can be imaged in-situ without magnetic inhomogeneities affecting the absorption profile. Near 804.5 MHz the threshold for quantum degeneracy is crossed. Our coldest experiments evaporate to 804.10, a mere 8 kHz above the trap bottom. Experiments probing this regime will be presented shortly, but first a word about the shape of the magnetic trap.

2.3.1 Magnetic trap characterization

The trap created from our Ioffe bars and coils has been studied in detail previously [46, 50]. Specifically, the trap frequencies were determined to be 50 Hz along the weak axial dimension and 3500 kHz along the transverse dimensions. A combination of parametric heating and modeling of magnetic fields was used. The accuracy of these characterizations is dependent upon our ability to tune the offset bias field of the IP trap to a specific value. Measuring currents and calculating the B field does not provide the needed accuracy so instead the value of minimum magnetic field in the trap is measured with RF evaporation.

The procedure for setting this minimum offset field, or trap bottom, is as follows. After loading into the IP trap, the atom cloud undergoes RF evaporation to 805 MHz. At that point, the RF is briefly turned off and quickly ramped to a lower value before turning back on and being held for 5 seconds. If the RF hold is below the minimum frequency of evaporation nothing will occur and the atoms will remain in the trap with observed losses being only those due to background gas collisions. However, if the held RF value is raised to the point where it is equal to or above the minimum evaporation frequency a hole will open in the magnetic trap. Atoms will leak out and only a small fraction will be left at the end of the experiment. Thus the experimental signature is a sharp transition in measured atom number at the point where our evaporation frequency is equal to the hyperfine splitting at the trap minimum. A sample scan is displayed in Fig. 2.11, where the trap bottom was set to 804.025. The trap bottom was set to 804.12 for all TOF experiments which follow in this chapter. For the majority of soliton work presented in subsequent chapters it was set to 804.025. This adjustment is merely for convenience and optimizing evaporation performance.

A further correction for gravitational sag is accounted for in [50], but this correction is only minimally relevant to the work presented here. What is significant is the characterization of the magnetic trapping potential: $\omega_z = 2 \times \pi \times 50$ Hz, $\omega_x = \omega_y = 2 \times \pi \times 3500$ Hz, and $\nu_{\text{bottom}} = 804.12$ Hz for TOF experiments and 804.025 for in-situ experiments. These carefully measured values are used in calculating derived quantities later.

2.4 TOF experiments and experimental signatures

After loading $\sim 10^9$ atoms of ${}^7\text{Li}$ into a magneto-optical trap, the atoms are optically pumped into the $|2S_{1/2}, F = 2, m_F = 2\rangle$ state and transferred into a cigar-shaped Ioffe-Pritchard trap with trapping frequencies $\omega_z = 2\pi \times 50$ Hz and $\omega_r = 2\pi \times 3.5$ kHz. Collisions between atoms in this state are characterized by a negative s-wave scattering length of $a = -27.6a_0$ (a_0 is the Bohr radius), which results in an effective attractive interaction between atoms [51]. Once in the trap, clouds are cooled using

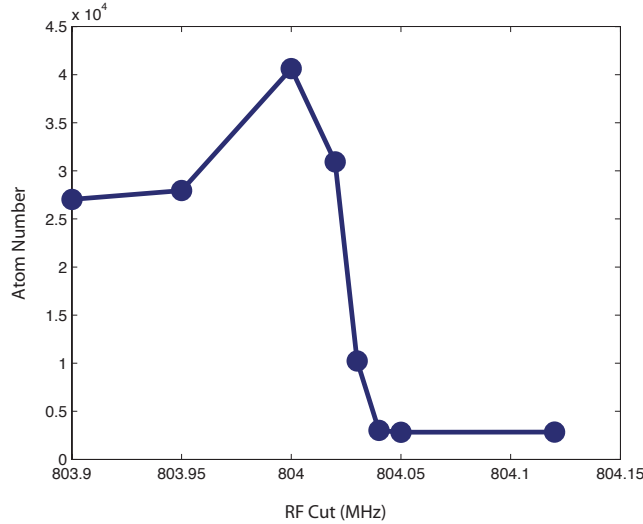


Figure 2.11: Curve indicating the minimum resonant RF evaporation frequency in the Ioffe-Pritchard trap is 804.025 MHz. This corresponds to a minimum offset magnetic field of 0.35 Gauss

forced radio frequency (RF) evaporation. Following the cooling cycle, cloud spatial distributions are imaged using an absorption imaging method. Example atom density distributions at different points in the evaporation sequence are shown in Fig. 2.12.

Absorption images are analyzed to extract atom number N_a and the *in-situ* axial and radial cloud widths, σ_z and σ_r . From these quantitites the peak atomic density, ρ_{pk} , the peak interaction energy per particle, $|\mu_{\text{int}}|$, and the total energy per particle, μ_{tot} (sum of kinetic, potential, and interaction energy), are estimated. Since we lack a theoretical model for the density of states in an harmonic potential when attractive interactions become significant, cloud temperature, \tilde{T} , is estimated from axial size alone. From \tilde{T} and the observed atom density, an effective phase space density (PSD), $\tilde{\zeta}$, and an effective fractional PSD, $\tilde{\zeta}/N_a$, are calculated. These are used as figures of merit for the quantum degeneracy of the gas. A brief description of the image analysis procedures for these experiments follows, after that some surprising behavior of the attractive Bose gas in quasi-1D traps is discussed.

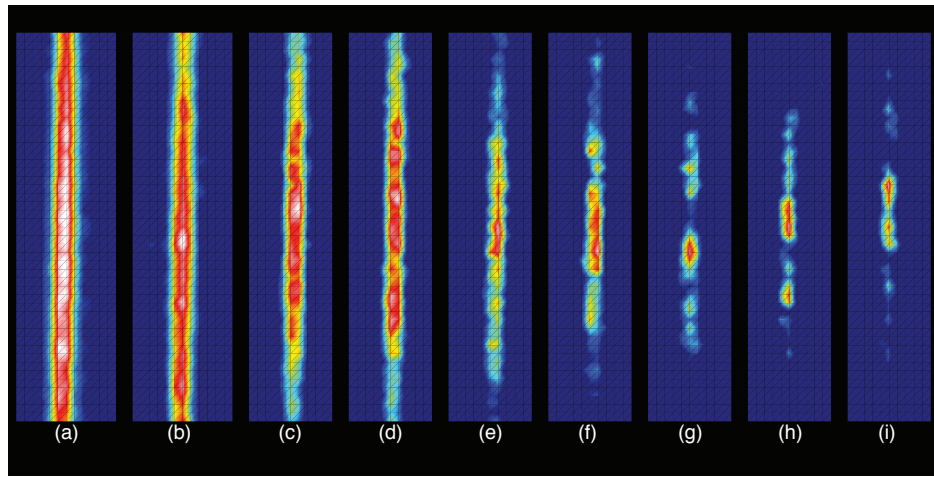


Figure 2.12: Atomic density distributions near the trap center at various points in the forced RF evaporation sequence. The final RF evaporation frequency, ν_f , in each image is: (a) $\nu_0 + 350$ kHz, (b) $\nu_0 + 180$ kHz, (c) $\nu_0 + 37$ kHz, (d) $\nu_0 + 19$ kHz, (e)-(h) $\nu_0 + 9$ kHz. Several images at the lowest RF frequency are included to demonstrate the variation in final density distributions. The corresponding numbers of atoms are (a) 1.7×10^5 , (b) 6.4×10^4 , (c) 3.0×10^3 , (d) 1.8×10^3 , (e) 3.0×10^2 , (f) 4.4×10^2 , (g) 4.4×10^2 , (h) 4.4×10^2 . Each pixel (indicated by grid lines) images a $5.8 \mu\text{m} \times 5.8 \mu\text{m}$ area. Finally, ν_f is the final RF evaporation frequency and ν_0 is the RF frequency corresponding to the trap bottom.

2.4.1 Data analysis for TOF experiments

For each atomic cloud I extract the relevant data from its absorption image, converted to an atom density profile. The density profile is fit to a Gaussian, from which I extract peak optical depth and axial and radial $1/e$ radii after ballistic expansion, $\sigma_{z,\text{TOF}}$ and $\sigma_{r,\text{TOF}}$, respectively. Using the measured ballistic expansion time and the measured imaging system point spread function $1/e$ radius, $\sigma_{\text{PSF}} = 4.8 \pm 0.5 \mu\text{m}$, I calculate the *in-situ* axial and radial cloud widths, σ_z and σ_r , using the following:

$$\sigma_i = \sqrt{\frac{\sigma_{i,\text{TOF}}^2 - \sigma_{\text{PSF}}^2}{1 + \omega_i^2 t_{\text{TOF}}^2}} \quad (2.4)$$

where $i \in \{r, z\}$.

Next, N_a , σ_z , and σ_r are used to calculate experimentally relevant derived quantities. The sum of the mean kinetic and trap potential energies per particle is

$$\mu_0 = \frac{1}{2}m(2\omega_r^2\sigma_r^2 + \omega_z^2\sigma_z^2) \quad (2.5)$$

The peak number density is $\rho_{\text{pk}} = N_a / (\pi^{3/2}\sigma_r^2\sigma_z)$. The per particle mean field interaction energy is

$$|\mu_{\text{int}}| = \frac{1}{2}\rho_{\text{pk}}g^{(2)}(0)4\pi\hbar^2|a|/m = 2g^{(2)}(0)\hbar^2|a|N_a/(\pi^{1/2}m\sigma_r^2\sigma_z) \quad (2.6)$$

where $g^{(2)}(0)$ is the two-body correlation function evaluated at zero separation. In Fig. 2.15 we use $g^{(2)}(0) = 2$, the value for a thermal cloud, for evaluating $|\mu_{\text{int}}|$ for our data points, which we believe are not in a pure state; however, we use $g^{(2)}(0) = 1$, the value for a pure state, in evaluating the $|\mu_{\text{int}}|$ collapse criterion because that theory applies to a singly occupied orbital. The total per particle energy is

$$\mu_{\text{tot}} = \mu_0 - \mu_{\text{int}} 2^{-5/2} \quad (2.7)$$

where one factor of 2^{-1} is a consequence of the quantum virial theorem for interacting particles and the remaining $2^{-3/2}$ converts from peak to average interaction energy per particle.

For non-interacting particles in a 3D harmonic potential, the temperature is given by

$$\tilde{T} = m\omega_z^2 \sigma_z^2 / 2k_B \quad (2.8)$$

where k_B is Boltzmann's constant; PSD is given by

$$\tilde{\zeta} = \rho_{\text{pk}} \tilde{\lambda}_{\text{dB}}^3 \quad (2.9)$$

$$\tilde{\lambda}_{\text{dB}} = \sqrt{2\pi\hbar^2/mk_B\tilde{T}} \quad (2.10)$$

is the thermal de Broglie wavelength for non-interacting particles.

2.4.2 Results

What is remarkable in the results presented so far is the lack of traditional Bose-Einstein condensation. The clouds in panels **c-i** of Fig. 2.12 should each be well below the condensation threshold for these atom numbers and temperatures; nonetheless, the atom distributions do not indicate a pure state. The distributions remain much wider than the predicted ground state size of this trap $l_z = \sqrt{\hbar/(m\omega_z)} = 5.6\mu\text{m}$, and show a high degree of variability from shot to shot. Still, the gas is not believed to be thermal, as calculated phase space densities place the atoms well into the quantum degenerate regime.

This is shown in Fig. 2.13 where standard BEC theory is used to predict the condensation threshold for our system, in the 3D and 1D limits [52]. Our experiment

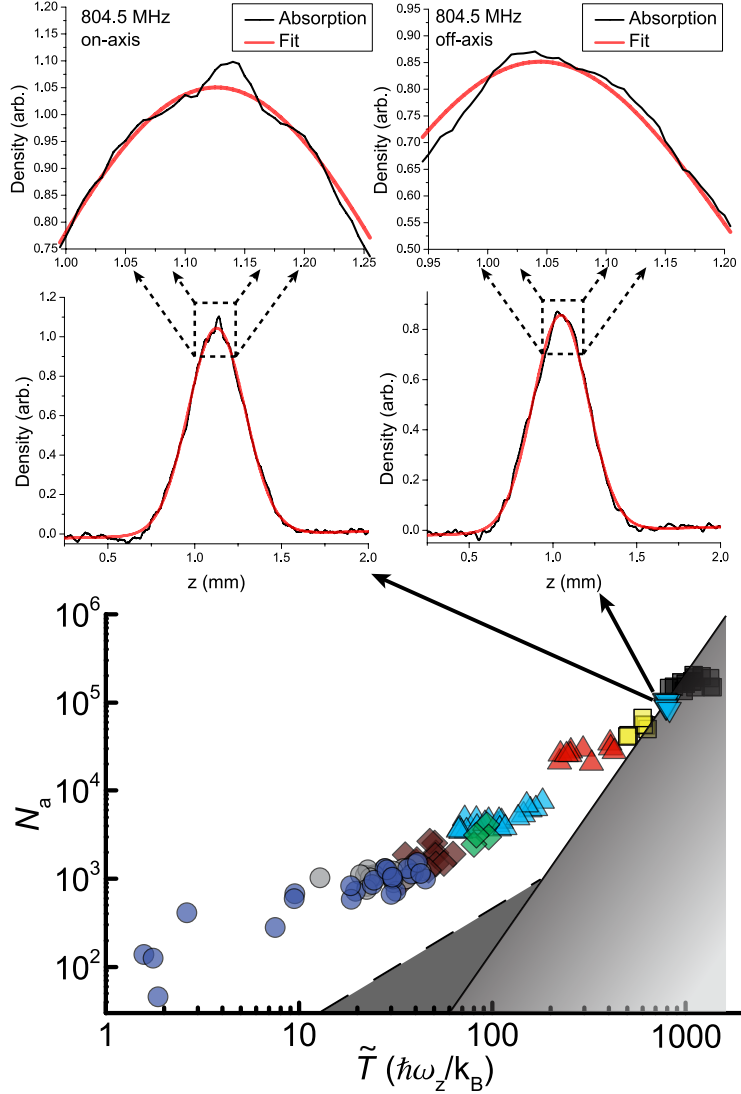


Figure 2.13: (a) Total atom number N_a as a function of temperature \tilde{T} (normalized to the axial mode spacing ω_z) and axial cloud width σ_z (normalized to the axial oscillator length, $\sqrt{\hbar/m\omega_z} = 5.4 \mu\text{m}$, where m is the atomic mass). The dotted and dashed lines mark the BEC transitions in the 3D and 1D regimes, respectively [52]. Insets are the averaged axial density profile for the points closest to the calculated 3D BEC transition (blue triangles), on center axis and off. One can clearly see a density spike on axis that is not present in the off-axis shots. This indicates an accumulation of atoms in or around the trap's ground state. Final RF evaporation frequencies, ν_f , are: $\nu_0 + 350 \text{ kHz}$ (black square), $\nu_0 + 200 \text{ kHz}$ (blue triangle down), $\nu_0 + 180 \text{ kHz}$ (yellow square), $\nu_0 + 110 \text{ kHz}$ (red triangle), $\nu_0 + 37 \text{ kHz}$ (blue triangle up), $\nu_0 + 30 \text{ kHz}$ (green diamond), $\nu_0 + 25 \text{ kHz}$ (black diamond), $\nu_0 + 19 \text{ kHz}$ (gray circle), and $\nu_0 + 14 \text{ kHz}$ (purple circle). Finally, ν_f is the final RF evaporation frequency and ν_0 is the RF frequency corresponding to the trap bottom

operates well within the quantum degenerate regime, producing atom clouds with high numbers and sufficiently cold temperatures to trigger condensation. Furthermore, as the 3D BEC threshold is crossed an increase in cloud density near the center of the trap is observed. An average of 5 density distributions for the RF closest to this transition point are displayed in Fig. 2.13 as well. This indicates the beginning of condensation and the resultant bimodal distribution at this point in our sequence. However, for some reason the process is frustrated and does not run to completion. Clearly the data avoid the two step condensation regime for non-interacting particles by passing well above the intersection of the 3D and 1D condensatin threshold curves [53].

Concurrent with crossing the 3D BEC transition is a rise in measured phase space density assuming a non-interacting particle model. The method for calculating this proxy for PSD, $\tilde{\zeta}$, is given above, and the results are shown in Fig. 2.14. Here both the total and fractional values are plotted, and one can see that $\tilde{\zeta}$ rises from 1.2 ± 0.1 at $\nu_f = \nu_0 + 180$ kHz (yellow square), to 4.3 ± 0.5 at $\nu_f = \nu_0 + 110$ kHz (red triangle), and exceeds 10 for $\nu_f < \nu_0 + 25$ kHz (black diamond) (ν_f is the final RF evaporation frequency and ν_0 is the RF frequency corresponding to the trap bottom). It is worth noting that the fractional PSD, $\tilde{\zeta}/N_a$ saturates near 0.1, indicating that a pure state is not formed [this is also evident from the density profiles (f)-(i) in Fig. 2.12]

As indicated in Fig. 2.15, we produce clouds where the interaction energy is substantially larger than the axial oscillator energy, but significantly smaller than the radial oscillator energy ($|\mu_{\text{int}}| \sim 5\hbar\omega_z \sim \hbar\omega_r/14$). Throughout evaporation the interactions are stronger than the axial mode energy splitting while still satisfying the stability criterion, $|\mu_{\text{int}}| < 1.95\hbar\omega_r$ [54]. As the expected low energy states are multiple solitons, with widths smaller than can be resolved with our imaging system, the inferred values of $|\mu_{\text{int}}|$ are likely a lower bound. The local interaction strengths could be as large as $140\hbar\omega_z$.

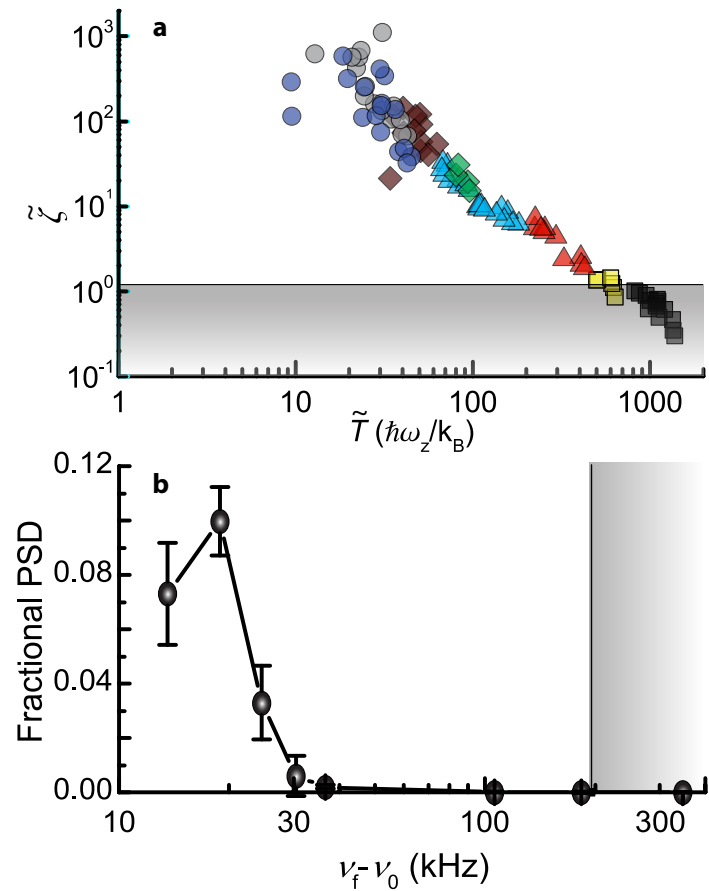


Figure 2.14: Phase space density $\tilde{\zeta}$ as a function of \tilde{T} (a). Phase space density divided by measured atom number vs RF cut (b).

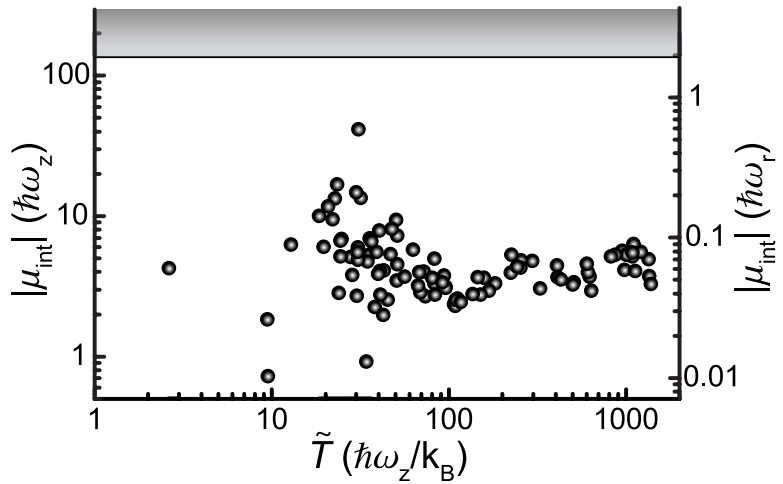


Figure 2.15: Peak interaction energy per particle (normalized to both the axial and radial mode spacings) as a function of \tilde{T} (normalized to the axial mode splitting). The horizontal dotted line at $|\mu_{\text{int}}| / \hbar\omega_r = 1.95$ indicates the collapse threshold. This data demonstrates that throughout our cooling evaporation sequence the peak interaction energy per particle is significantly greater than the axial mode spacing while remaining suitably below the radial mode spacing so that the clouds remain stable against collapse.

2.4.3 Theory of fragmentation

The exact spectrum for an attractively interacting 1D Bose gas with longitudinal freedom is derived in [55]. The corresponding many-body eigenstates are groups of solitons. Though within solitons the atoms are tightly bound, distinct solitons do not interact with each other. The ground state, a single momentumless soliton containing all N_a atoms, is the exactly-solved analog of the ground state solution predicted by the mean-field Gross-Pitaevskii (GP) equation [56, 55]. In this framework, the coldest clouds reported here can be interpreted as excited states consisting of overlapping solitons; however, imaging resolution limits our ability to distinguish individual solitons.

The model described above relies on the generalized Bethe *ansatz* and the assumption of a strictly 1D system. Such systems are integrable and will not thermalize [57]. In contrast, the observed atomic clouds appear to thermalize, even at the lowest temperatures – as the gas is evaporatively cooled deep into the quasi-1D regime, ζ continues to grow. We note, however, that our system does not satisfy the Bethe *ansatz* and that it is only quasi-1D, with the finite radial confinement leading to a density dependent nonlinearity in a soliton’s chemical potential. Furthermore, the finite extent of a soliton’s mean-field potential enables three-body scattering events, where two free-particles collide in the presence of a soliton. Under these conditions, a mixture of free thermal particles and a single soliton are predicted to come into thermal equilibrium in highly anisotropic traps [58].

This formalism also applies to scattering events leading to soliton growth and decay in a thermal bath. Theoretical estimates of these rates for our experimental parameters indicate that the number of atoms in each soliton stabilizes at values significantly below the collapse threshold, thus frustrating a growth/collapse cycle and allowing continued growth of PSD. Additional effects are predicted to appear beyond a mean-field description of the system which further limit the growth of a single soliton. For example, the multiconfigurational time-dependent Hartree for bosons (MCTDHB) formalism predicts bifurcation of single solitons [59, 60]. The MCTDHB method has also recently been used to demonstrate dynamical fragmentation between a pure state of multiple solitons. The loss of coherence between these solitons leads

to a repulsive short range force that prevents the bound states from passing through one another [30].

2.4.4 conclusion to TOF experiments

Taken together, these are important revisions to either GP theory or a strictly 1D many-body theory. They provide clear indications that excited states of multiple solitons will be long lived and possibly in equilibrium with the background vapor and each other. Our observations are consistent with these predictions, and suggest that these states emerge naturally from a simple evaporative cooling protocol.

In summary, we have created a superluminescent matter wave source by evaporatively cooling attractively interacting ^7Li to quantum degeneracy in a quasi-1D trap. Future work may seek to exploit the coherence properties of these states for improving atom interferometric devices.

Chapter 3

Deterministic Single Soliton Production

In the previous chapter, it was seen that direct evaporation of ${}^7\text{Li}$ did not produce the known ground state, which is a single lone soliton located at the trap's center. We believe this to be due to the high aspect ratio between the axial and transverse dimensions of the minitrap. To compensate for this, all future experiments are performed with the final stage of evaporation occurring in a hybrid optical magnetic trap. A red detuned beam of 852 nm is directed along the magnetic trap's transverse axis and focused to a spot size with $1/e$ diameter of 25 μm . When this beam is raised to full power AC stark shifts deform the local axial potential, and a hybrid trap with $\omega_z = 2\pi \times 1.0 \text{ kHz}$ is created. This allows us to cross the 3D condensation threshold in a trap with aspect ratio much closer to 1 than before, 3.5:1 instead of 70:1. This process and consequent results are described in further detail below; however, the critical point is that the use of this hybrid potential allows for the formation of a pure single soliton at a particular point in space inside the Ioffe-Pritchard trap.

3.1 The optical trap

A 80 mW DBR laser with wavelength 852 nm is used to create an optical trap beam. This light is sent through an acousto-optic modulator and the +1 order is aligned to

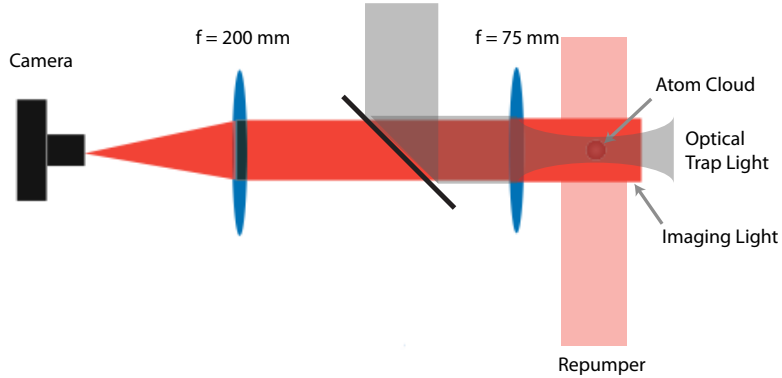


Figure 3.1: Diagram of the imaging system with optical trap beam added. The dichroic is used during normal operation to protect the CCD camera, but is removed for initial alignment. The optical dipole trap (ODT) beam must be run at low power during this procedure.

a non-polarization maintaining fiber. The output is sent through a polarizing beam splitting cube, for clean up and the light is then directed to a telescope system that focuses the light on the atoms inside the magnetic trap. After being sent through the cube for polarization clean up, but before entering the telescope for focusing a pick-off beam sampler is used to direct a small sample of light to a monitoring photodiode. This measured power is then fed back to a PI control circuit which matches the laser power to a preset given by the computer. This setup allows for a beam of known polarization, controlled power, and fixed size and position to address the atoms.

The beam is aligned parallel to the imaging light and directed towards the Andor Ixon CCD. Under normal operation a dichroic is used to deflect the IR beam and protect the camera's chip from the 20 mW beam with focus at the atom position; however, during the initial alignment phase this piece of the imaging path is removed so that the trap beam can be aligned to the atom cloud with aid of the camera. This portion of the optical setup is displayed in Fig. 3.1. Using this method we are able to achieve good alignment between the trapping beam and our atoms, as well as directly measure the size of our focus, which is $\approx 25 \mu\text{m}$. A screen shot of the first time atoms were successfully optically trapped in this system can be seen in Fig. 3.2.

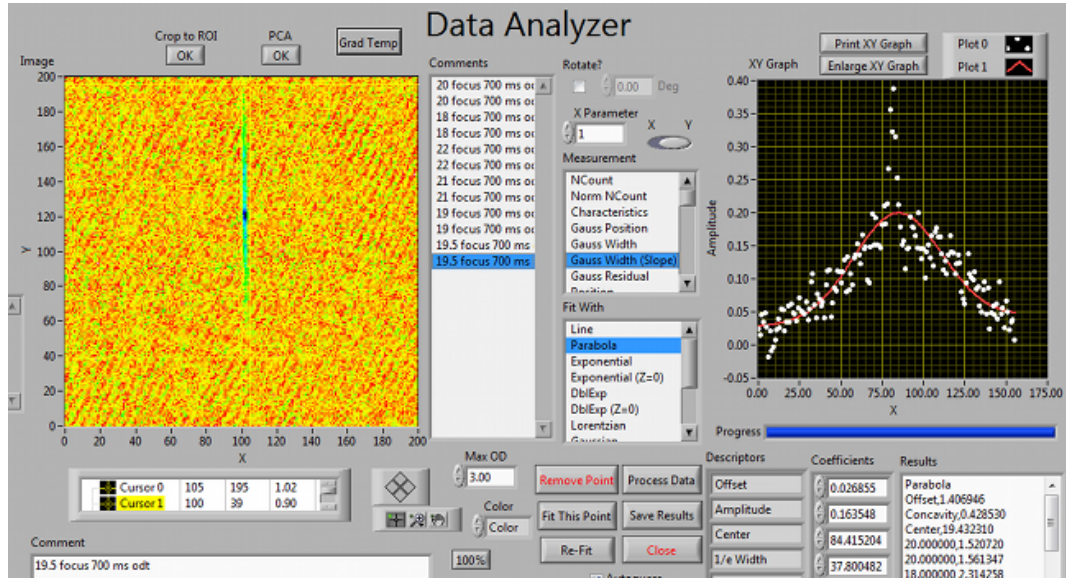


Figure 3.2: Screen capture of imaging control station during the first successful load of our optical trap.

It is important to characterize the hybrid magnetic-optical trap, as this information is crucial to future experiments. By knowing the total power directed at the atoms, the frequency, and the spot size we are able to estimate the trap's depth and frequency by use of the theory of AC stark shifts (reference Metcalf). Atoms bathed in far red detuned light are subject to an attractive potential of the form.

Nonetheless it is worthwhile to experimentally verify these numbers. The atoms themselves can be used to characterize the effective potential directly. By turning the optical beam up to full power and determining when our ability to contain all the atoms is exhausted, we achieve a good measure of the full trap's depth. A picture of this turning point can be seen in Fig. 3.3. The RF cut used to generate this image was 120 kHz above the trap's bottom. Our previously calibrated η factor of 6.7 gives us an estimate of the thermal energy, and thus the trap's depth, of 25 kHz.

Another important characteristic is the frequency of oscillation for atoms at the bottom of the trap. By knowing this we will be able to estimate zero-point energy as well as the wave functions of atoms held there. This value is determined through

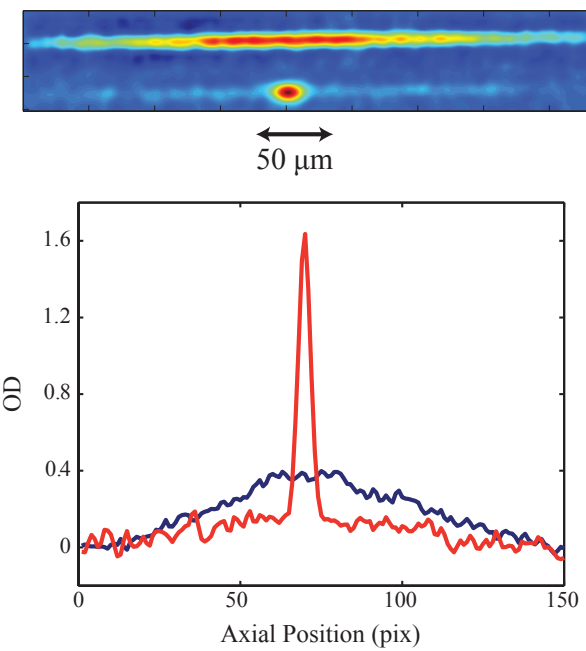


Figure 3.3: 2D absorption images and integrated axial profiles of cold atoms. The elongated image is taken without the optical trap beam, while the rounded image has the ODT raised to full power.

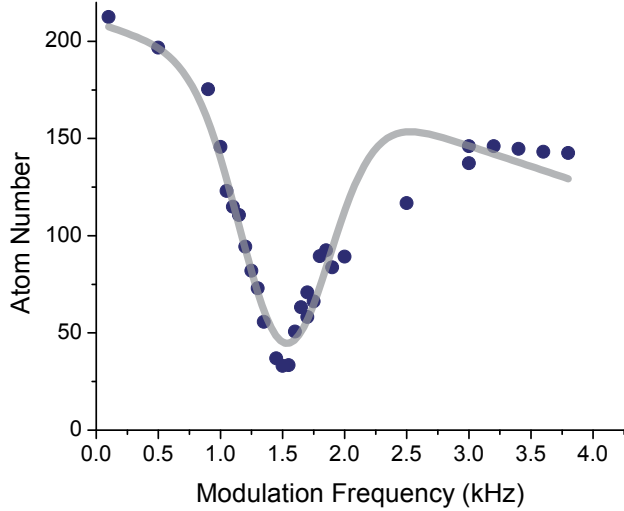


Figure 3.4: Scan of modulation frequency of the optical trapping beam. Center of dip is measured to be 1.54 ± 0.03 kHz, indicating a ground state frequency of 770 ± 15 Hz. For these experiments the optical trap beam was set to 2/3 full power.

parametric heating of the trapped atoms and locating a resonance. Atoms are evaporated to just before the point of Bose condensation and the optical trap beam is then amplitude modulated at a particular frequency for 1 second. The number of atoms remaining in the trap after this procedure is then recorded. The frequency of modulation is scanned until a dip corresponding to resonant heating is located. Empirically, this value was found to be near 1.54 kHz for an optical trap at 2/3 full power (13.3 mW). Due to the even symmetry of direct amplitude modulation the trap's ground state frequency must be half of this measured value. This is because the form of excitation used here must necessarily drive transitions between the ground and second excited state, rather than the ground and first excited state. A scan of atom number vs modulation frequency for these parameters is shown in Fig. 3.4. As a final check the ODT's power was halved and the scan was repeated. The resonant frequency was observed to follow the scaling of $\omega P^{1/2}$, where P is the power in the trapping beam; this agrees with theory.

3.2 Seeding condensation

The optical trap is raised for the final 1.4 seconds of evaporation. The increased axial trapping frequency during this final step increases the density and collision rate dramatically. It also ensures the formation of a single pure soliton by avoiding the mismatch between the energy scales of the cloud’s chemical potential and mode spacing of the axial trap states, as was the case in previous experiments presented here. The dependency of pure state formation on trap aspect ratio have been studied theoretically previously [61, 60]. By virtue of this experimental setup, a single pure bright soliton can be formed under direct evaporation. This is a key difference between these experiments and previous work with bright atomic solitons where a Feshbach resonance was used to ramp the interactions of atoms inside a BEC from repulsive to attractive, a non-adiabatic step [15, 16, 17]. Furthermore, the anchoring of the soliton’s position to our optical trap allows for its formation at any location of my choosing inside the quasi-1D magnetic waveguide.

After evaporation is complete, the trap can be lowered adiabatically to release the resulting soliton for 1D time-of-flight (TOF) experiments. It has been found empirically that an exponential ramp with a $1/e$ ramp time of 0.5 ms is sufficient to not dramatically excite the soliton’s internal or external degrees of freedom. Atoms are imaged absorptively, and these images are integrated along the transverse direction to generate an axial profile. Images of the atoms after 100 ms time-of-flight show a clear bimodal distribution, as seen in Fig. 3.5. At high RF cuts and low optical trap depths, the solitons are accompanied by a significant thermal fraction. By contrast, at sufficiently low RF and stiffer optical traps, most thermal atoms are eliminated, leaving a pure single soliton. It is worth noting that this characteristic bimodal distribution which has become the signature of Bose-Einstein condensation has never before been seen with such resolution in a system with attractively interacting atoms. Solitons produced in this manner are long lived, with a $1/e$ lifetime of 6s. This is the same lifetime as we measure for a cold thermal cloud, indicating that the lifetime is likely limited only by collisions with the background gas. The measured atom number for short times of flight is found to be close to 100 atoms. Solitons of this occupancy

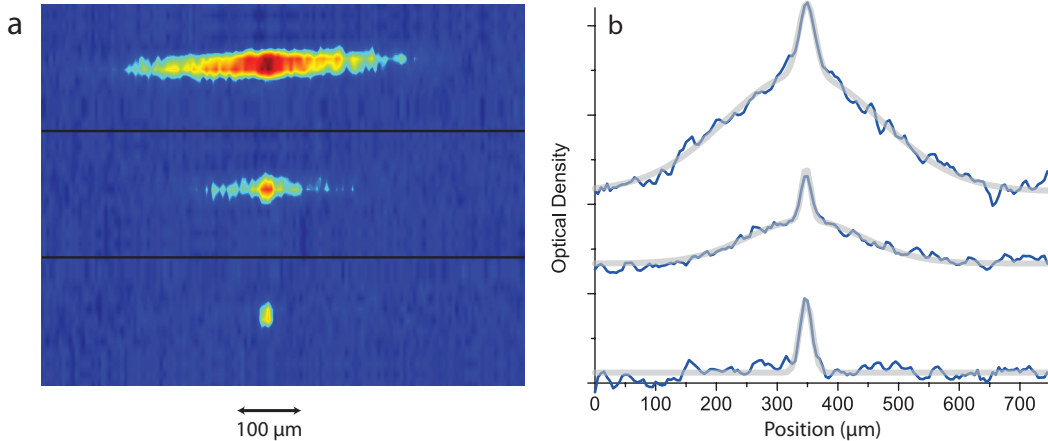


Figure 3.5: Atom density profiles for 2D absorption and integrated 1D axial after release from the optical trap and 100 ms TOF. The RF cut is lowered by 90 kHz between the top and bottom panels. As the resultant temperature drops, the profiles go from a clear bimodal distribution with high thermal fraction to a single pure soliton.

are predicted to have a spatial size only $1.6 \mu\text{m}$ which is below the system's imaging resolution of $9 \mu\text{m}$.

3.3 Soliton TOF experiments

3.3.1 Propagation without dispersion

The ability to propagate without dispersion in 1D potentials is the principle defining characteristic of bright solitons. Such behavior can be viewed with this system for various 1D potentials. For propagation in an harmonic trap, the optical trap is aligned $75 \mu\text{m}$ from the bottom of the axial center position, and the soliton is released for 1D TOFs. The trap geometry can also be modified to create a locally expulsive potential near the trap center as well. This is achieved with the use of a blue detuned laser beam ($\lambda = 532 \text{ nm}$), which is aligned parallel to the imaging and optical trap beams. By focusing the light to a spot size of $130 \mu\text{m}$ a broad positive potential can be created. This can be used to flatten the axial curvature near the trap's center, or create a

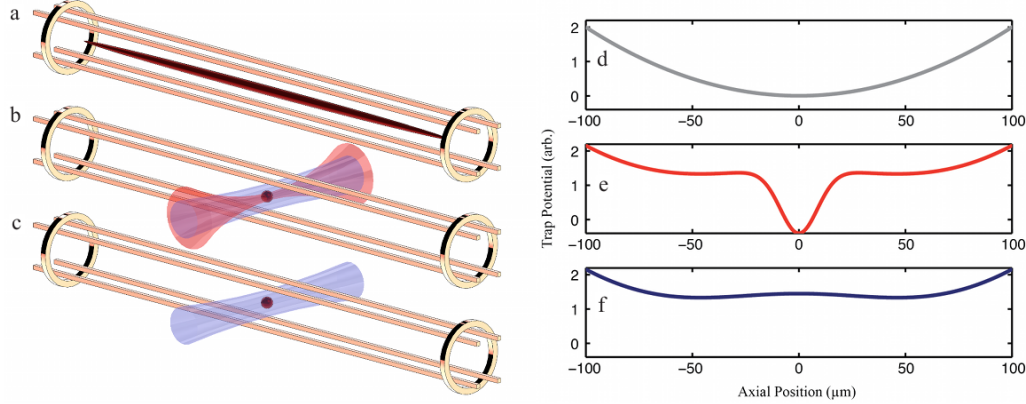


Figure 3.6: The experimental setup (**a - c**) as well as hybrid trap potentials (**d - f**) are diagrammed. First the atoms are evaporated in a custom Ioffe-Pritchard trap to a point just before quantum degeneracy would occur (**a** and **d**). Optical trapping and axial potential modifying beams are then turned on and a soliton is formed under direct evaporation (**b** and **e**). Finally, the optical trap is switched off adiabatically and the soliton is left to propagate in a 1D potential of our choosing, the case shown is when a broad blue detuned beam is used to generate a weakly explosive potential near trap center(**c** and **f**).

"w-shaped" 1D potential that is explosive in the center ($|\omega_z| = 2\pi \times 13$ Hz typically, and confining away from the center. The experimental procedure for the case where the magnetic axial potential is flattened near the trap's center is diagrammed in Fig. 3.6, and hybrid potentials are plotted along side. The results of 1D time-of-flight experiments that show propagation without dispersion for both the harmonic and explosive "w-shaped" cases can be seen in Fig. 3.7. The gas is able to propagate for 200 ms without any change in observed shape.

3.3.2 phase diagram of soliton production

Further experiments have been performed to determine the temperatures and trap shapes necessary to seed the formation of a single pure soliton. For these, the focus of

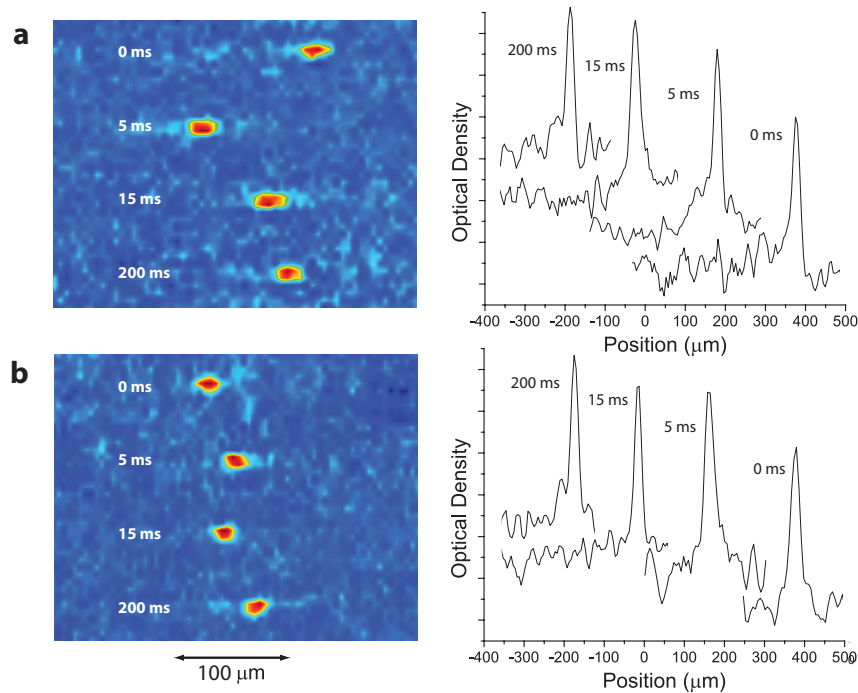


Figure 3.7: Absorption images and axial profiles of solitons after various 1D times of flight in an harmonic magnetic waveguide (a) and an expulsive optical and magnetic waveguide (b). Solitons are prepared in an optical trap, then released adiabatically into the waveguide. The images are integrated vertically to produce axial profiles. Each picture is the average of 5 shots. Axial profiles are offset horizontally and vertically for clarity.

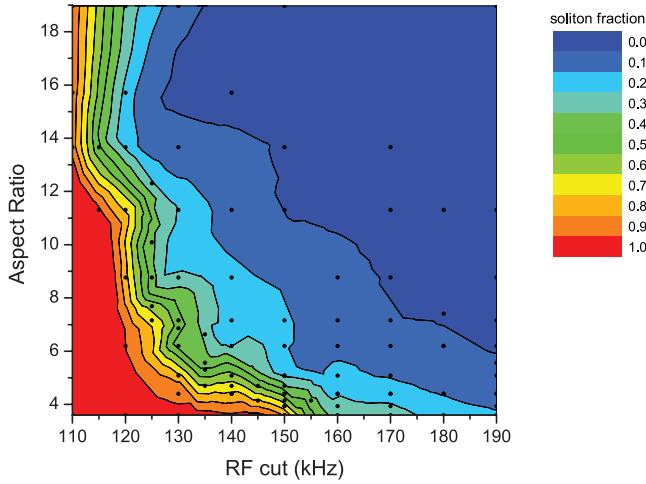


Figure 3.8: Phase diagram of condensate fraction as a function of RF cut and trap aspect ratio. Atoms are released for 100 ms TOF, then imaged absorptively. The soliton fraction is then extracted by fitting the 1D density profile. Measured data are smoothed by interpolation to generate the figure.

the optical trap is aligned to the bottom of the magnetic potential and the RF cut and optical trap power are scanned as experimental variables. To good approximation, the RF cut sets the temperature of the system, while the ratio of the transverse magnetic trap frequency to the optical trap frequency determines the aspect ratio during the final stage of evaporation. After 100 ms time-of-flight the atoms' axial density profile is measured. A bimodal distribution is fit with two Gaussian curves to determine the percentage of atoms inside the soliton (see Fig. 3.5 as examples). Although the shape of the soliton is predicted to be a sharply peaked hyperbolic secant [62], our finite imaging resolution renders the shape indistinguishable from a narrow Gaussian profile. Plotting the measured soliton fraction vs RF cut and trap aspect ratio gives a phase diagram for soliton formation, shown in Fig. 3.8.

The range of trap shapes that lead to the formation of a single pure soliton is not fully understood theoretically. While pure states are predicted to be the ground state in a spherically symmetric potential [61], fragmented states are predicted in the one-dimensional limit [60, 63]. This experiment is able to map directly, and for

the first time, the transition in behavior between these two limits. From the phase diagram in Fig. 3.8, it is clear that traps with aspect ratios as low as 2 and as high as 6 support single soliton formation with negligible thermal fraction. Formation of pure single solitons is not possible for trap aspect ratios significantly above 6, in qualitative agreement with the prediction of fragmentation in the one-dimensional limit [50].

3.4 Conclusion

These experiments outline a procedure for producing single solitons that can be easily implemented in other apparatuses. In addition, the characterization and description of output state provided here can provide a roadmap for future experiments that require a clean and well understood initial quantum state. Examples of such directions include the use of solitons for nonlinear atom interferometry and quantum information protocols. Indeed, the remaining experiments described in the following chapters, which are thematically related to these long term goals, will rely heavily on pure single soliton production as well as the mesoscopic quantum state's single particle like behavior.

Chapter 4

Macroscopic dynamics with bright solitons

At this stage, the quantum state that can be produced in the hybrid magnet-optical trap system is well understood. Our protocols support the production of a mesoscopic quantum bound state with $N \approx 100$ atoms. What's more, though very complicated, the object will behave as a single coherent particle under many experimental conditions. In this chapter, I describe experiments that take advantage of this fact to create what is believed to be a non-local quantum superposition state of these bright solitons. The state is believed to maintain coherence for separations of $70 \mu\text{m}$. This is accomplished by beginning with a bright soliton of initial size $\sigma_z = 185 \pm 3 \text{ nm}$ and releasing it into a one-dimensional waveguide. The center of mass wave function will undergo expansion due to initial momentum uncertainty. The resultant quantum object is predicted to be an expanding continuous distribution of bright soliton position states. I measure statistically the width of this distribution to be $\sigma_z = 23 \pm 5 \mu\text{m}$ after 60 ms time-of-flight. Nonetheless, detection of the atoms with resonant light produces an image of a single pure soliton with $N \approx 70$ atoms and a width $\xi \leq 10 \mu\text{m}$ for each individual experimental trial. This is consistent with projection of a mesoscopic non-local superposition state by a destructive measurement protocol. Additionally, the measured expansion rate of the center of mass wave function appears to be the minimum possible, predicted by Heisenberg's Uncertainty Principle for a soliton of

this mass. From measurements of soliton lifetime, I estimate that dephasing is not significant for these time scales, and that the inferred superposition state can exist without collapsing prior to measurement. This result holds promise for future cold atom experiments involving massive particle interferometry and tests of the limits of entanglement.

4.1 Experimental procedure

4.1.1 Setup and Procedure

The apparatus remains the same as described in the previous chapter; however, for the experiments presented here the blue detuned $\lambda = 532$ nm light is used to balance the magnetic trap's curvature near its center. This is done by setting the amplitude of this beam such that the second order term of the resulting potential's Taylor series will cancel with the magnetic trap's potential near $z = 0$. This will result in a confining potential whose lowest order term is quartic:

$$V = \frac{1}{2}m\omega_z z^2 + V_b \quad (4.1)$$

$$V = \frac{1}{2}m\omega_z z^2 + A\sigma^2 e^{-z^2/\sigma^2} \quad (4.2)$$

$$V = \frac{1}{2}m\omega_z z^2 - \frac{1}{2}Az^2 + \frac{A}{2\sigma^2}z^4 + O[z]^5 \quad (4.3)$$

$$(4.4)$$

Where V_b is the potential due to the Gaussian barrier, A is the gaussian beam's amplitude divided by its width, σ . By setting the amplitude to be $A = \frac{m\omega^2}{2}$ the net potential will become

$$V = \frac{1}{2}m\omega^2\sigma^2 \left(\frac{z}{\sigma}\right)^4 + O[z]^5 \quad (4.5)$$

$$(4.6)$$

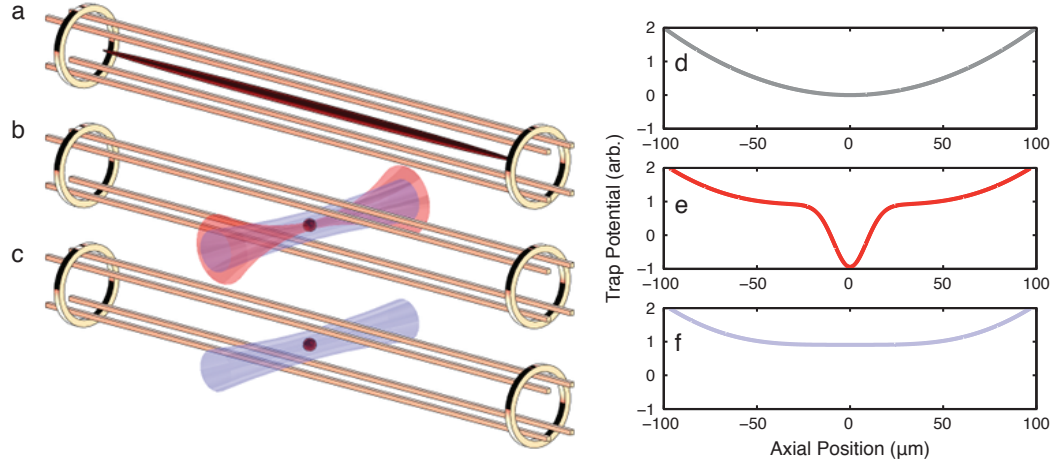


Figure 4.1: The experimental setup (**a - c**) as well as hybrid trap potentials (**d - f**) are diagrammed. First the atoms are evaporated in a custom Ioffe-Pritchard trap to a point just before quantum degeneracy would occur (**a** and **d**). Optical trapping and axial potential modifying beams are then turned on and a soliton is formed under direct evaporation (**b** and **e**). Finally, the optical trap is switched off and the soliton is left to propagate in a 1D potential of our choosing, the case shown is when a broad blue detuned beam is used to cancel the magnetic potential near trap center(**c** and **f**).

This is diagrammed in Fig. 4.1 where the experimental sequence and resulting hybrid magento-optical potentials can be seen.

4.1.2 Procedure for waveguide flattening

Another important control is to balance the magnetic trap's axial curvature with the expulsive potential of our blue detuned laser. If the blue beam is too weak the residual axial curvature will decelerate the atoms and reduce our signal. However, if the blue beam is too strong the atoms see an expulsive potential near the waveguide center and accelerate away from their release point, giving us a spurious expansion. To control for this we adiabatically release the atoms and look at their position after

20 ms free expansion. For this type of release we should see no measurable expansion in a flat waveguide. We then gradually raise the power in the blue beam until the standard deviation of cloud position shows measurable expansion. This transition point is where the local potential first becomes weakly expulsive near the trap center. We set the strength of our blue detuned beam to just below this for our experiments.

4.2 A macroscopic quantum single particle

What is remarkable is that this collection of atoms which behaves as a single massive particle can still exhibit quantum non-local behavior. We demonstrate this by suddenly releasing the gas and observing a spread in measured soliton positions that extends well beyond the soliton size. This effect is driven by the quantum limited uncertainty in the soliton's momentum wave function. To understand this process, it is important to note that the soliton's initial size is well known. The optical confining potential of $\omega_z = 750$ Hz is greater than the temperature at the end of evaporation, ensuring that the gas resides in the trap's ground state mode. To the extent that the soliton can be treated as a single massive particle, it will have a characteristic size inside the optical trap given by $\sigma_z = \sqrt{\hbar/(2m_{\text{sol}}\omega_z)}$ and reside in a minimum uncertainty state. If the optical potential is then switched off suddenly, the soliton will enter the magneto-optical waveguide described above with well defined spread in initial position and center of mass momentum given by Heisenberg's Uncertainty Principle $\sigma_z\sigma_p \geq \frac{\hbar}{2}$, where σ_p is the uncertainty in center of mass momentum. The initial size, and corresponding spread in initial momentum, can be set arbitrarily by slowly ramping the optical confining potential from 750 Hz to some other value of ω_z before releasing the atoms. One last consideration for this procedure is that the atom density distribution of the soliton in the trapped and free configurations are sufficiently similar. This problem has been studied previously where it was found that for trap aspect ratios greater than 10 the overlap between initial and final soliton states was better than 90% [64]. The transverse frequency of our magnetic trap is fixed at $\omega_\rho = 2\pi \times 3500$ Hz; consequently, we should release solitons from axial traps with frequency below 350 Hz to maintain good overlap between initial and final quantum

states.

Once the gas is released, the center of mass wave function will expand in the nearly flat magneto-optical potential, Fig. 3.6f, with a minimum expansion rate given by $v = \frac{\hbar}{2m_{\text{sol}}\sigma_z}$. For our experiments, we suddenly release from an optical trap with $\omega_z = 300$ Hz which corresponds to a minimum expansion rate of $v = 0.35(1)$ $\mu\text{m}/\text{ms}$. After 60 ms time-of-flight the width of the center of mass wave function is predicted to be 21 μm , much larger than the predicted soliton size $\xi = 2.2$ μm . In the absence of decoherence, the gas exists in a mesoscopic non-local superposition state until our measurement protocol projects the soliton to a particular location. Signatures of this behavior can be seen in Fig. 4.2b where over several trials the position of the soliton jumps from one location to another. This is contrasted with a control experimental sequence in which the optical trap is slowly ramped to 0 before the time-of-flight, Fig 4.2a.

This experiment is modeled using GPE code. The initial state prior to sudden release from our optical trap is found using imaginary time evolution and the nonlinear Schrödinger equation one dimension. Wave function evolution from a cloud with initial size corresponding to a snap release from a 300 Hz trap is compared with that of a cloud with initial size of 5 μm in Fig. 4.3. While the cloud which is initially larger in size shows very little change of extent over an 80 ms simulation, the cloud which is initially confined expands quickly and is even turned around by the weak axial curvature at $t = 40$ ms. The parameters used for this simulation are close to the ones of the experiments presented here, with $N = 70$ atoms and initial sizes to as best as we can estimate.

The expansion of the soliton's position wave function is a quantum mechanical effect that can only be seen statistically. Consequently, we collected more than 100 individual measurements of solitons released from a 300 Hz trap after 60 ms time of flight. A histogram of the position of each soliton can be seen in Fig. 4.4. From this, we observe that the soliton's center of mass wave function spans approximately 75 μm and has filled the flat region of our waveguide. Nonetheless, for each individual experiment the measured soliton size is $\xi \leq 10$ μm indicating that the atoms remain in a single quantum state that is well localized; note that the soliton size is predicted to be much

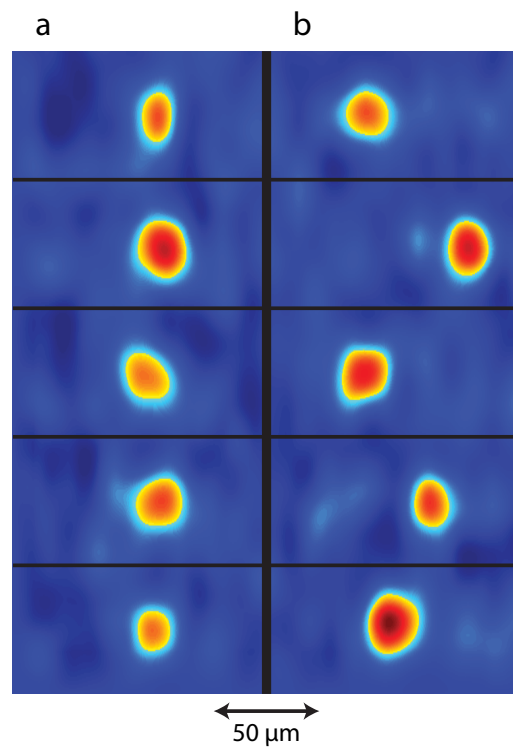


Figure 4.2: Absorption images of our bright atomic solitons after 60 ms of free expansion in the magneto-optical waveguide. In **a** the solitons were released adiabatically from the optical trap. In **b** the optical trap was set to have a trap frequency of $\nu = 300$ Hz and then switched off in 10 μ s.

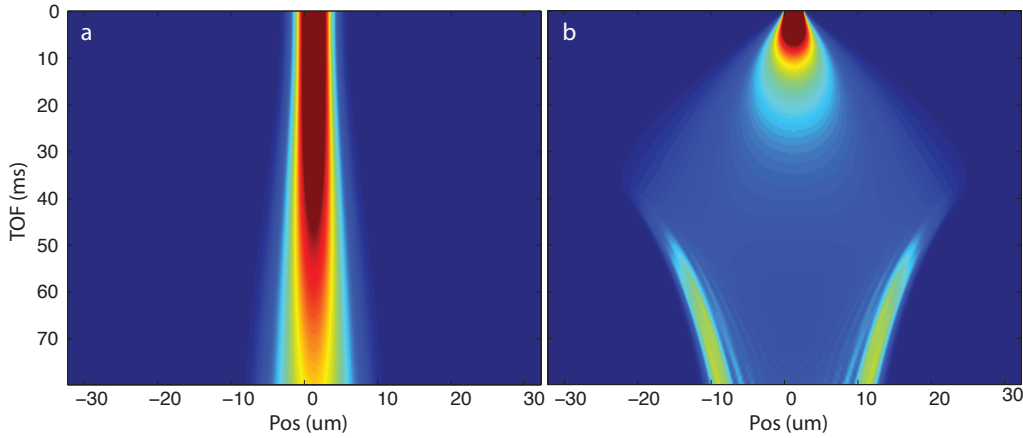


Figure 4.3: Two simulations of the one dimensional nonlinear Schrodinger equation investigating the expansion of a soliton’s center of mass wave function with time. The cloud can be given an initial size of $5 \mu\text{m}$ (a) or 185 nm (b). For the case of stronger initial confinement a large expansion of the state’s wave function is observed in the sub 100 ms time scale.

smaller, but the system’s imaging resolution limits our ability to accurately measure this value. These results build up a picture of the modulus squared of the wave function, which can be thought of as an expanding superposition of a continuum of soliton positions. This interpretation is supported by a cursory analysis of dephasing time in the many-body superposition state, which is calculated to have a value $\tau = 150 \text{ ms}$. This estimate comes from a measurement of the soliton lifetime in our trap and the average soliton occupation number. We find that the soliton lifetime is limited by collisions with the background gas and has a value of $\gamma = 6.5 \text{ s}$. Additionally, the soliton occupation number is measured to be $N = 70 \pm 15$ for these trials. We have assumed a worse case scenario of the non-local Schrödinger’s Cat state completely decohering with the loss of a single atom. This yields a dephasing time of the form $\tau = \frac{\gamma}{N(1-e^{-1})}$.

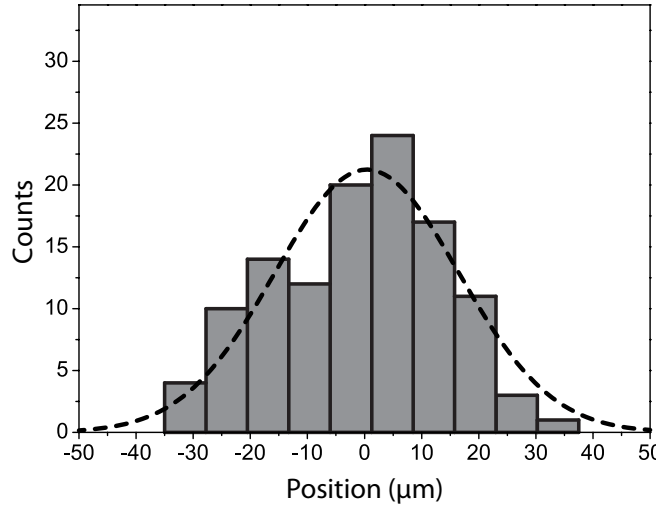


Figure 4.4: A histogram of 119 shots of soliton position after 60 ms time of flight. The soliton was snap released from a 300 Hz optical trap and the wave function expanded into a flat magneto-optical waveguide. The distribution is fit to a gaussian with a $1/e$ width of 22.8 μm .

4.3 Measuring wave packet expansion

4.3.1 Heisenberg limited wave packet expansion

In additional experiments, we measure the width of the distribution of soliton positions for several different times of flight and calculate a rate of expansion. This can then be compared with the theoretical value given by our assumed minimum uncertainty wave-packet and Heisenberg's Principle. We perform these experiments for solitons released using both the slow and sudden procedures. For each expansion time, the individual shots are averaged and a Gaussian width is fit to the cumulative atom distribution. The measured expansion for a snap release from a trap of 300 Hz is $v = 0.36 \pm 0.03 \text{ mm/s}$. Release without snapping yields an expansion rate of $v = 0.026 \pm 0.007 \text{ mm/s}$, more than 10 times smaller than that of the snap-off procedure. This lower velocity represents the limit of our ability to adiabatically release from a trap of finite size as well as balance the curvature of the magnetic trap with the broad blue detuned beam. These two different expansion rates are plotted

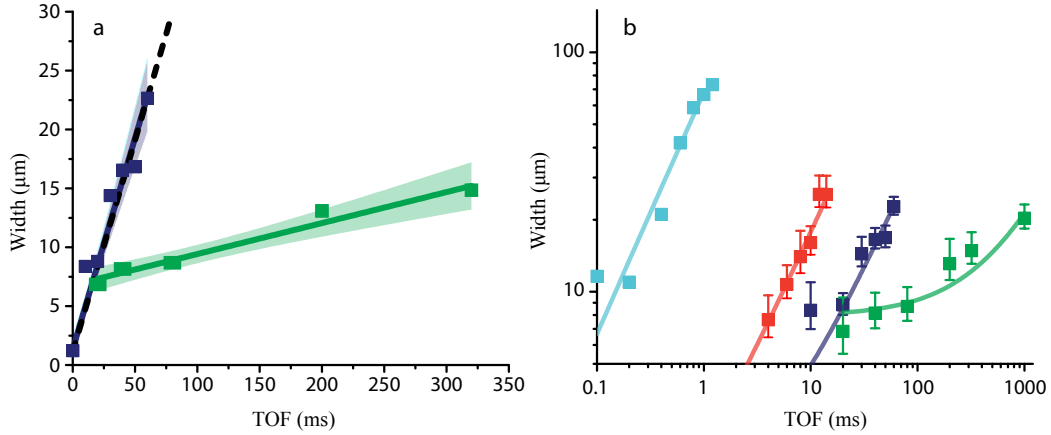


Figure 4.5: A graph of measured width of the average atom distribution vs free expansion time. Plotted in **a** are experiments involving sudden releases from a 300 Hz trap (navy) and 10 ms releases from a 750 Hz trap (green). The shaded regions represent a 95 % confidence band on the linear fits to the data. Additionally, a theoretically predicted expansion rate from Heisenberg's Uncertainty Principle with zero free parameters is plotted for the 300 Hz snap release experiments (dashed). Four experiments were plotted on a log-log scale in **b**: A snap release from a 300 Hz optical potential (navy), a 10 ms ramp from 750 Hz to 0 Hz (green), a release of thermal atoms (light blue), and a snap release from 735 Hz (red). The 1σ statistical error bars are shown here.

in Fig. 4.5a, and the expansion of solitons released with the fast procedure is also compared with theory. The measured velocity agrees well with a predicted velocity of 0.35 ± 0.01 mm/s. As stated above, this theoretical value is, $\Delta v = \frac{\hbar}{2m_{\text{sol}}\sigma_z}$, and it is calculated using our mean measured soliton occupation of 70 atoms, $m_{\text{sol}} = 70 \times m$, as well as the initial size a particle with this mass has in the motional ground state of a 300 Hz harmonic trap, $\sigma_z = \sqrt{\frac{\hbar}{4\pi \times 300 \times m_{\text{sol}}}} = 185 \pm 3$ nm. Both the measured soliton occupancy and the optical trap characterization are independently determined leaving the fit to theory with zero free parameters (Supplementary information).

It is also instructive to consider a release of hot thermal atoms from our optical trap. These atoms will be unbound and travel at much higher velocities due to both their increased kinetic energy, which is set by the temperature of the RF cut rather than the zero point energy of the optical trap, and their lighter mass. From the

strength of the RF cut (ν_{RF}) and the Virial theorem we can predict the speed with which atoms should fly away from the waveguide center, $\frac{1}{2}k_B T = \frac{1}{2}\hbar\nu_{\text{RF}} = \frac{1}{2}mv^2$. For RF cuts 70 kHz above trap bottom we predict an expansion velocity of $v = 62.9$ mm/s, and we measure the expansion rate to be $v = 70 \pm 10$ mm/s, which agrees well. These different expansion rates are plotted in Fig. 4.5b, with all three regimes: snap release, adiabatic release, and thermal atoms being clearly distinguishable.

4.3.2 Questions of Adiabaticity

An important consideration not yet addressed is the number of internal modes excited in the soliton by the sudden trap opening. To the extent that this occurs, the released gas will not be a pure soliton, but instead will have some average number of excitations corresponding to occupied phonon modes. If this number is too high, we would expect the soliton to break up after release. This number was calculated explicitly for the limit of $\mu_0 > \hbar\omega_z$, and was found to be:

$$N_{\text{ex}} \approx 0.1446 \times N \left(\frac{\hbar\omega_z}{\mu_0} \right)^4 \quad (4.7)$$

Where $\mu_0 = -\frac{mg_{1\text{D}}^2}{8\hbar^2}$ is the soliton's untrapped chemical potential and $g_{1\text{D}} = 4a\hbar\omega_p N$ is the 1D atom-atom coupling constant [65]. From this, we estimate a minimum soliton occupancy of $N = 100$ atoms is required to ensure that $N_{\text{ex}}/N < 0.1$. Our experiments do not meet this criterion, thus we can expect some experimental runs to have significant heating, which can manifest as the image of an exploded soliton at the end of time-of-flight. We account for this by post-processing our data to only include shots where a single clear and distinct soliton is observed. This procedure guarantees that in each run we report the heating was not significant. Furthermore, recall that in an harmonic trap the center of mass and internal soliton degrees of freedom are separable; consequently, excitation of the soliton's internal modes should not affect the expansion rate of the center of mass wave function reported above.

The sudden release of the soliton can be simulated numerically on a computer. We use the split operator method to solve a one-dimensional Gross-Pitaevskii field

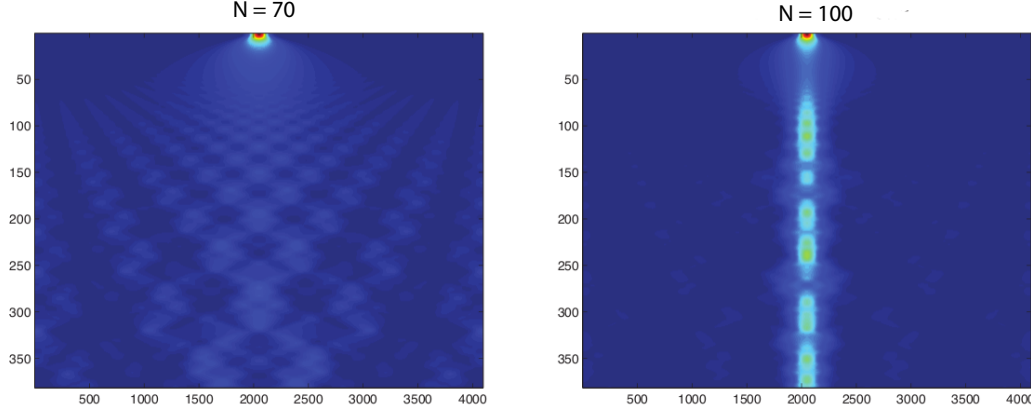


Figure 4.6: Probability densities for states suddenly released from a 300 Hz trap with $N = 70$ and $N = 100$ atoms respectively. The $N = 70$ case exhibits sufficient excitations to cause break up, indicating that experiments run with these parameters will require post processing.

equation for different experimental parameters. Imaginary time evolution is used to find the ground state wave function of a soliton with N atoms inside a trap of $\omega_z = 2\pi \times 300$ Hz. This state is then released and the atom density profile is recorded during a short time of flight. The simulation is run for $N = 70$ and $N = 100$ atoms. Significant heating is seen for the case of $N = 70$, but not for the $N = 100$ case. This is inline with the analytic approximation provided in [65]. Once again, we compensate for these excitations by post processing the recorded data to only include shots where a pure soliton is observed.

4.3.3 Stronger initial confinement

Lastly we conducted experiments with a snap release from stronger optical traps. The expected initial size change is sub-linear with optical trap power, $\sigma_z \sim \omega_z^{-1/2} \sim P^{-1/4}$, where P is the optical trap power. Consequently, a large change in optical trap intensity is required to observe statistically significant changes in the expansion rate. Empirically, we find that the optical trap's power cannot be increased beyond a factor of 2, $\omega_z = 430$ Hz before predicted and measured expansion rates begin to diverge; this

is not surprising as we estimated a threshold for sufficient overlap between trapped and untrapped states of 350 Hz earlier. For optical traps stronger than this the measured expansion rate outpaces the Heisenberg predicted value. Solitons are still being observed upon measurement implying that the bound state remains intact; however, the faster than expected expansion indicates that the atoms no longer occupy a minimum uncertainty state inside the trap. This can occur if system nonlinearities cause the atom distribution to become strongly non-gaussian. A graph of measured expansion for an optical trap with $\omega_z = 735$ Hz is also plotted in Fig. 4.5a, its rate lies between the high speed thermal atoms and the well controlled solitons released from weaker potentials. The energy spread associated with this expansion velocity is $\frac{1}{2}m_{\text{sol}}v^2 = \frac{1}{2}\hbar\Delta\nu$, where $\Delta\nu = 3$ kHz.

4.4 A potential interferometer or double slit experiment

The remarkable robustness of these Lithium solitons stands out in these experiments. The projection of 70 atoms to the same point in space with each measurement is a clear indication of the particles behaving collectively as a single quantum object. Repeated measurements allow one to directly probe the many body wave function in an elegant demonstration of quantum mechanics on a many particle scale. Furthermore, we have demonstrated a degree of control of the quantum object's position and momentum limited only by the Heisenberg Uncertainty Principle. We anticipate a multitude of new research directions for bright atomic solitons. One potential extension of our work is to create a soliton interferometer from the quantum limited many particle input state we have described here. This would be relevant for future experiments in entangled state interferometry as well as long time interferometry [66, 15].

Chapter 5

Multiple Soliton Production and Experiments

It is now possible to exploit the interactions between ultracold atoms for the production of novel many-body quantum states. Techniques include the use of Feshbach resonances as well as the manipulation of an external trapping potential for bright atomic soliton production [15, 16, 17, 67]. These solitons occur in one-dimensional (1D) systems where the attraction between atoms exactly cancels the dispersive and diffractive effects of wave-packet localization, leading to the formation of a mesoscopic quantum bound state [22]. The coherence properties, mesoscopic size, and long lifetimes of solitons make them an attractive candidate for experiments involving nonlinear atom interferometry [26, 66] and quantum information storage [27, 28, 68]. These applications often rely on coherent single particle like behavior of the many-body quantum state. Experiments with colliding solitons can simulate dynamics relevant to these applications and offer well defined tests to probe their theoretical underpinnings. Specifically, multi-soliton experiments can study the limits of effective 1D theories for 3D nonlinear systems [31, 58, 69] and test the validity of mean field models in systems where quantum fluctuations may lead to fast decoherence [70].

5.1 Motivations for moving beyond previous work

Previous experiments with multiple bright atomic solitons were performed with ^7Li and ^{85}Rb [15, 16, 17]. After the formation of a BEC in a highly anisotropic optical trap, a Feshbach resonance was used to switch the atom-atom interactions from repulsive to attractive. This procedure resulted in the production of a stochastic soliton train. Multiple collisions without any spatial overlap were observed, and these dynamics were described by Gross-Pitaevskii (GP) theory for a uniform 1D system with an assumed π phase shift between adjacent solitons [71]. Additional phenomenology has since been predicted with models that account for the breaking of 1D symmetry by external confining potentials, or more fully treat the 3D dynamics of bright solitary matter-waves [72, 73, 69, 58, 31]. Effects of interest include spatially overlapped solitons and collisional induced soliton collapse [62], phase dependent mass and/or momentum transfer [72, 33], and soliton-soliton fusion [32, 69]. Each of these effects has been seen in systems with optical solitons propagating in fibers [74, 75]; however, we believe we are the first to report their observation in a matter-wave system.

5.2 Creating distinct solitons

We begin with a cloud of ^7Li atoms in the $|F, m_f\rangle = |2, 2\rangle$ state, held in a cigar shaped Ioffe-Pritchard trap. The experimental apparatus has been described previously [67]. Solitons form under direct evaporation due to the weak attraction between atoms in this state, characterized by a short range negative scattering length $a = -27.6a_0$ (a_0 is the Bohr radius) [51]. The majority of evaporation is done in a highly anisotropic Ioff-Pritchard trap with $\omega_x = \omega_y = 2\pi * 3500$ Hz and $\omega_z = 2\pi * 50$ Hz; however, solitons are seeded during the final stage of evaporation at select positions with the aid of a red-detuned $\lambda = 852$ nm laser focused onto the atom cloud. The light is directed transverse to the magnetic trap and focused to a spot size of $25 \mu\text{m}$ 1/e diameter. A near retro-reflecting mirror is used to create a second focus of similar size but displaced axially along the atom cloud. The light creates an extra potential at each focus that increases the local axial trapping frequency from 50 Hz to 1.0 kHz

at full power. Each atom is confined to one of these two hybrid traps, ensuring the formation of a single soliton at each focus position. Lastly, our final RF cut is chosen to eliminate any residual thermal atoms.

After evaporation has been completed, the optical traps are lowered adiabatically and the solitons will slosh in the magnetic trap. A requirement for observing effects not seen in previous matter-wave experiments is for the solitons to be overlapped for a sufficient amount of time. This corresponds to having a relative kinetic energy that is approximately equal to, or less than, the soliton binding energy [31]. To control for this in our experiment, we use a spatially broad, blue-detuned beam ($\lambda = 532$ nm) to minimize the weak axial curvature of the trapping potential; this allows us to lower the initial potential energy difference between solitons while maintaining separations that are resolvable with our imaging system. The beam is aligned parallel to the optical trapping beams and is focused to a spot size of $130 \mu\text{m}$ $1/e$ diameter in the plane of the atoms. We estimate a reduction of the trap's axial curvature by at least 80% over this length scale, for details see [76]. The atoms undergo a 1D time-of-flight (TOF) in this hybrid magneto-optic potential before resonant light is directed along the transverse axis for absorptive imaging.

5.3 Collision experiments: two solitons

5.3.1 Creation and initial collision

For our experiments, one optical trap was placed at the center of the magneto-optic waveguide and the second was displaced $50 \mu\text{m}$ from this position. Upon release, the residual axial curvature of the guide causes the soliton displaced from the center to move inward, where it collides with the stationary soliton. We measure the relative velocity for this collision to be $v_{\text{rel}} \approx 17 \text{ mm/s}$. The moving soliton appears to pass directly through the stationary object before turning around in the magnetic trap and repeating the process. Fig. 5.1 displays the first pass between these two solitons in a sequence of images taken 1 ms apart. No significant transfer of atoms or momentum is observed after this first collision; nonetheless, the two matter waves

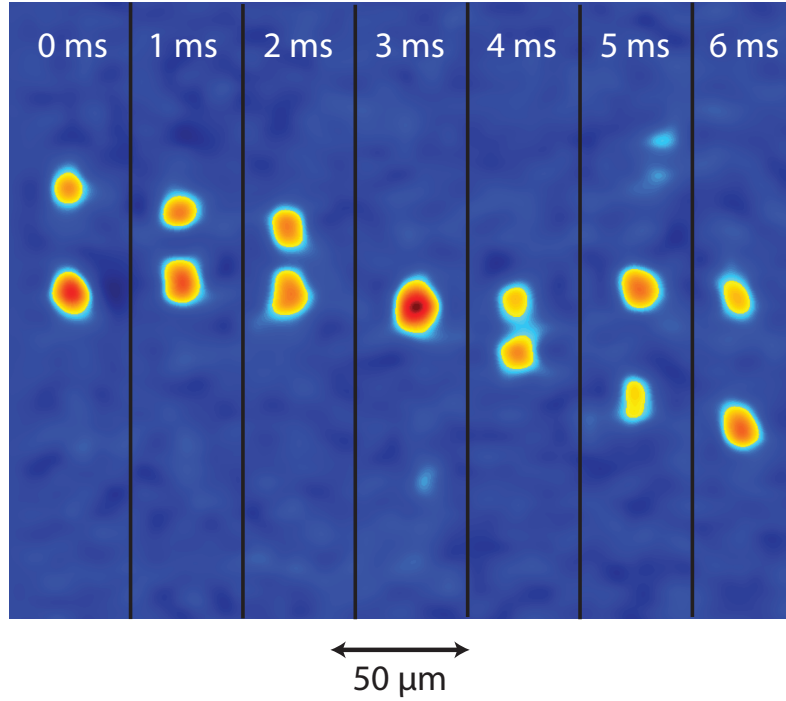


Figure 5.1: Two independent solitons are formed in optical traps and then released into the magneto-optic waveguide at $t = 0$. The higher positioned soliton begins to move downward and collides with the lower soliton near the waveguide's center. There is a measured increase in local density when the solitons briefly overlap at $t = 3$ ms, before becoming well separated again at $t = 5$ ms.

clearly overlap, indicating a relative phase $\Delta\phi \approx 0$. This is in sharp distinction to previous experiments with colliding bright atomic solitons.

5.3.2 Phase dependent collisions

When solitons overlap during a collision the local density increases dramatically. This can lead to the exchange of mass and momentum from one soliton to the other. Numerical simulations of the 3D Gross-Pitaevskii equation predict mass transfer between solitons which varies as $\sin(\Delta\phi)$, where $\Delta\phi$ is the relative phase between the matter-waves [33]. We approximate this theory as an effective 1D nonlinear Schrödinger

equation with terms out to 5th order, following the steps outlined in [58]. Specifically, we use an equation of the form:

$$i\hbar \frac{\partial \psi}{\partial t} = \left[\hat{T} + U + g |\psi|^2 + g_2 |\psi|^4 \right] \psi \quad (5.1)$$

Here, \hat{T} is the kinetic operator, U is the external trapping potential, and g is the atom-atom coupling term derived from a 1D GP theory that ignores excitations in the tightly confined radial dimensions. Lastly, g_2 is a correction term required when the mean-field interaction grows comparable to the energy spacing of the radial modes, and the assumptions used to derive g breakdown. This will occur for colliding solitons when the sum of the individual populations is close to, or above, the critical atom number required for collapse. Results of a simulation showing phase dependent population transfer are depicted in Fig. 5.2a. Soliton's with different initial phase will undergo different trajectories, finally arriving at different positions for long TOFs. An example of the effect changes in initial phase can have on final soliton position is shown for a simulated 80 ms TOF in Fig. 5.2b.

For each experimental run, we expect there to be a random initial phase between solitons, $0 < \Delta\phi < 2\pi$. Consequently, the momentum transferred with each collision will also vary from shot to shot. This will lead to a growing uncertainty in each soliton's center of mass wave function with increasing time of flight. We are able to observe this effect as a large spread in measured soliton positions for TOFs greater than 100 ms. This can be seen in Fig. 5.2c where the positions of the initially moving soliton is plotted vs the position of the initially stationary soliton for $t = 120$ ms. As expected the positions of the solitons are correlated with each other, with a correlation coefficient of 0.68. For our sample size of $n = 24$, this represents a 3.7 sigma rejection of the possibility that this perceived correlation is due to random fluctuations. As a control against parametric heating or center-of-mass wave function dispersion, individual solitons were released into the wave guide one at a time and no such increase in uncertainty was seen. For 120 ms TOFs, the uncertainty in measured position was larger by a factor of 2.25 for solitons that underwent multiple collisions.

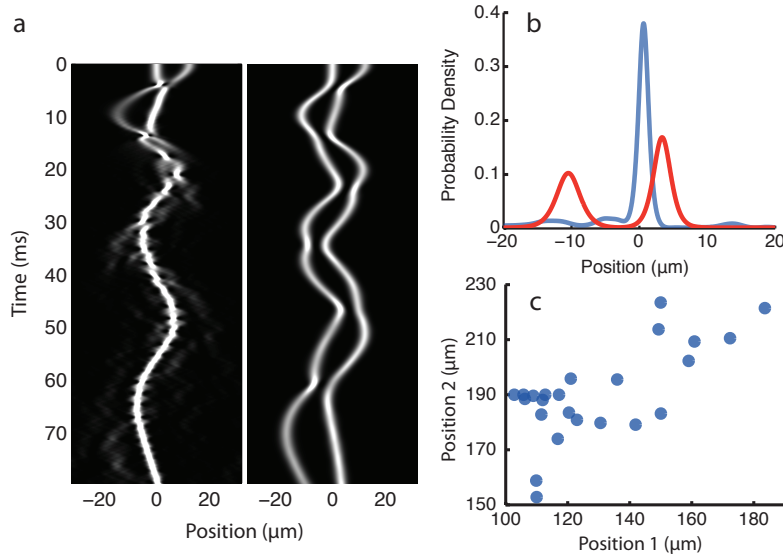


Figure 5.2: 3D Gross-Pitaevskii simulation of soliton collisions with 0 and π relative phase (**a**). Solitons are created at $t = 0$ with occupations $N = 0.6N_c$ and $N = 0.5N_c$, where N_c is the critical atom number for our magneto-optic waveguide. For the case of 0 relative phase, the local density increases beyond the point where the system can be approximated as truly one-dimensional, the collisions become inelastic, and mass is transferred from one soliton to the other. For the case of π relative phase, the local density is suppressed during soliton overlap, and the collisions remain elastic. The alternate trajectories lead to different probability distributions for soliton positions at time $t = 80$ ms (**b**). Experimental data showing the measured positions of two clear and distinct solitons at $t = 120$ ms are also shown (**c**). Multiple collisions with phase dependent momentum transfer cause the observed positions to be correlated and spread over a large region.

5.3.3 Soliton-soliton fusion

A second effect of interest, also predicted by 3D GP theory and effective 1D theories with non-integrable quintic Schrödinger equations, is the fusion of two solitons into a single object [31, 77, 69]. This effect is the limiting case of the incremental mass transfer described above. For two solitons approaching with relative velocities below some critical threshold there exists a range of relative phase, centered around $\Delta\phi = 0$, where solitons are expected to merge. For the specific case of $\Delta\phi = 0$ the critical velocity has the following dependencies: $v_c \propto N^3$ and $v_c \propto \omega_r^2$, where N is the total atom number and ω_r is the radial trapping frequency [69]. For our experimental parameters we estimate the critical velocity to be $v_c = 6.8$ mm/s, or roughly half the initial relative velocity. We have already established that mass and momentum are transferred incrementally between solitons for collisions with appropriate relative phase, thus causing the relative velocity to drop with each successive collision. This creates a simple picture, where for certain initial relative phases and atom soliton occupations, we would expect to observe soliton fusion after multiple collisions. To test for this we take multiple shots at $t = 120$ ms and count the number of solitons present. In 50 trials we measure the probability of observing two clear and distinct solitons to be 0.52. The remainder of the time there is only one soliton. Images showing the results of individual experiments are displayed in Fig. 5.3. Ultimately, it is impossible to tell if these fused solitons were produced incrementally over the 11 collisions for this TOF or were the product of a single merging event.

It is important to exclude the possibility that solitons we believe to have merged are not merely overlapped. The destructive nature of imaging makes it impossible to simply image the merged soliton again at some later time. Instead, we verify the observation of soliton-soliton fusion by studying the atom loss rate. As stated above, a small number of atoms are ejected from the solitons during each collision. This can be measured and quantified for different times of flight. Once the individual solitons merge, atoms will no longer be lost in this way. Instead, the decay rate will depend only on background gas collisions. The measured lifetime curve is displayed in Fig. 5.4a and clearly shows this two step nature. The slowly decaying tail has the same lifetime, to within error bars, as pure single solitons released into our trap,

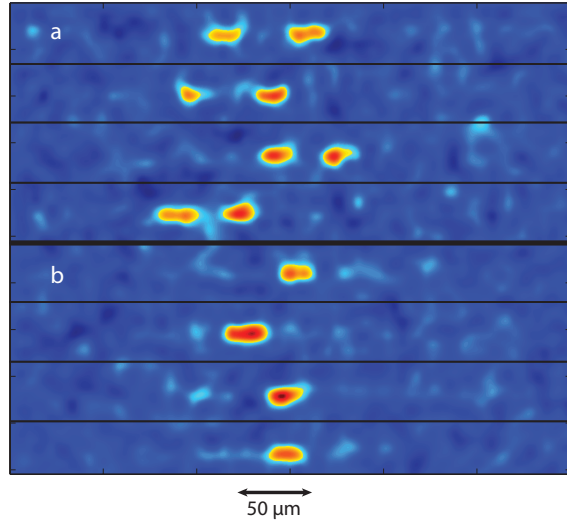


Figure 5.3: Absorption images of solitons after 120 ms time-of-flight demonstrate stochastic merging behavior. Images with two distinct solitons are displayed in **a**. Images with only one soliton are shown in **b**.

$\tau = 6.5$ s. In addition, we can post process the data to only look at runs where two solitons live until the end of TOF. This data is inset in Fig. 5.4a and shows a fast loss of atoms that agrees with the initial decay seen in total atom number for the aggregate, $\tau = 230 \pm 40$ ms and $\tau = 170 \pm 30$ ms respectively.

Atom number fluctuations offer an additional signature of soliton merging events. Post processing images by the number of observed solitons gives two separate distributions of total measured atom number. If the observed single soliton pictures were simply two overlapped solitons, one would expect the two distributions to be similar. However, this is not the case as seen in the histograms of these distributions plotted in Fig 5.4b-c. We measure a mean atom number for merged solitons of $\mu = 126 \pm 7$ atoms, which differs significantly from the mean atom number measured for two solitons, $\mu = 156 \pm 4$. Uncertainties quoted are standard errors. The measured standard deviations also differ by nearly 45%, $\sigma = 33.5$ for the merged case and $\sigma = 23.3$ for the distinct soliton case. We expect some atoms to be shed during the soliton fusion process in order to satisfy energy and momentum conservation. This would

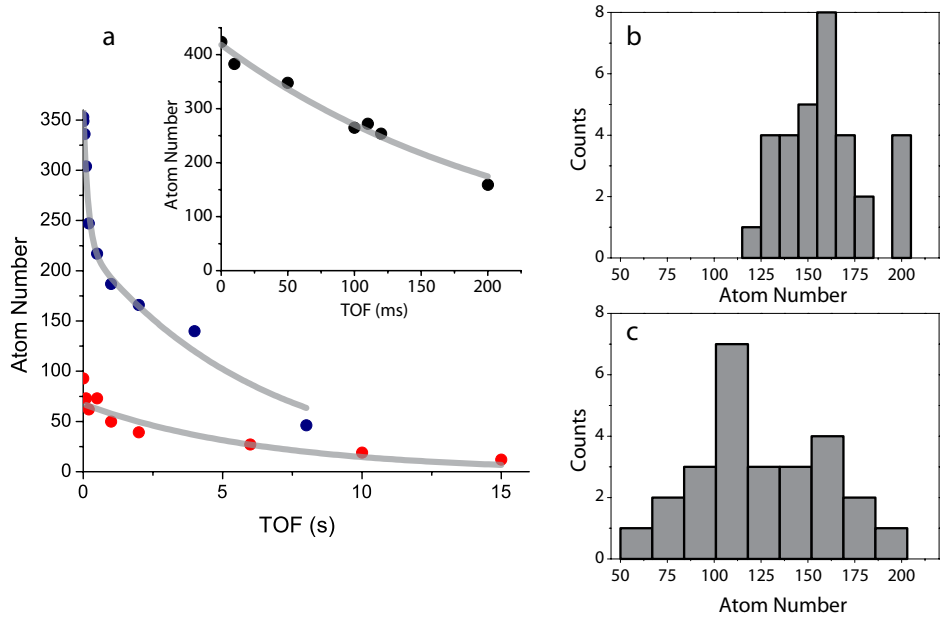


Figure 5.4: Atom lifetime curves for soliton time-of-flight experiments (**a**), two soliton collision experiments (navy) and single soliton lifetime measurement (red). Mutlisoliton collisions exhibit a two step loss of atoms. Approximately half of the atoms are lost quickly with a lifetime of $\tau = 170$ ms. The remaining atoms are lost more slowly with a lifetime of $\tau = 6.3$ s. This agrees with the measured single soliton decay time, $\tau = 6.5$ s. A lifetime curve generated from a subset of two soliton collision experiments is inset in (**a**). Only shots where two solitons survived to the end of TOF were used. The decay in atom number agrees with the fast decay measured for the entire data set. Distributions of measured atom number for $t = 120$ ms time-of-flight experiments are plotted for the cases with two solitons (**b**) and one soliton (**c**). Centers and spreads of the distributions are different, $\mu_{1\text{sol}} = 126 \pm 7$ and $\mu_{2\text{sol}} = 156 \pm 4$.

account for the lower mean atom number, and increased standard deviation, of the fused soliton's atom number distribution.

5.4 Conclusion

To conclude, our ability to produce two independent solitons with a random phase difference and low relative velocity grants us access to an experimental regime previously unrealized in atomic systems. We observe significant spatial overlap of two solitons during collision, indicating a relative phase of $\Delta\phi \approx 0$. These high density collisions initiate dynamics that cannot be explained with conventional 1D Gross-Pitaevskii theory, including momentum transfer between solitons and soliton-soliton fusion. In this fully 3D regime, we confirm that bright solitary matter-waves behave in a manner well described by 3D Gross-Pitaevskii theory or the quintic Schrödinger equation. Experimental observations that these strongly interacting many-body quantum states, operating near the limit of self-induced collapse, can be treated as coherent single-particle objects is an important result. Important not only in the validation of these theories, but also for future experiments seeking to build on the coherent particle like properties of these states. Such future directions include using collisions to induce entanglement between two solitons [78] and tests of decoherence in many-body atomic systems due to quantum fluctuations [70, 79].

Chapter 6

Conclusion

Experiments with ultracold Lithium atoms have been presented above. Our success at overcoming initial frustrations in the formation of pure BECs and cooling to the gas to its quantum ground state, a single soliton, has led to several advancements in cold atom physics. The controlled production of bright solitons has paved the way for future experiments with these remarkably robust super-particles. Our measurements of life-time and observed propagation without dispersion holds promise for future campaigns seeking to exploit these objects as a bright source of coherent particles. Furthermore, in the experiments described in this thesis the quantum nature of these objects has been directly demonstrated.

The first demonstration of a soliton's wave like nature was achieved by observing expansion of the center-of-mass position in a nearly flat waveguide. This experiment represents the first half of a Young's double slit experiment with bright solitons, the coherent diffraction from a single slit. The state's expansion rate was measured to be the minimum possible given by Heisenberg's Uncertainty Principle, the calculated initial localization, and the soliton mass. This process represents a kind of "quantum machine" where the soliton is moved from an initial position to a final distribution of positions by the creation of a massive non-local Schrödinger's Cat. Repeated trials are consistent with measurement induced quantum state projection. The absence of any fragmentation in many shots and our favorable estimates as to the dephasing time are causes for optimism in the interpretation of these results.

A second probe of the boundary between wave like and particle properties of the quantum soliton was performed in our collision experiments. Two independent solitons were formed and released with a relative velocity roughly double the critical velocity predicted to cause collapse or soliton-soliton fusion. The coherent wave-like character of these super-particles was seen in observed mass and momentum transfer as well as random soliton-soliton fusing events. These phenomena point to a need for 1D mean field theories beyond the Gross-Pitaevskii framework for accurate description and prediction; however, they also validate the use of mean-field theories as a valid approximation of the full quantum description for these experimental parameters. The observations were verified by a thorough analysis of decreased soliton lifetime during collision experiments, an marked correlation between final soliton positions, and an analysis of number fluctuations for merged and distinct solitons. These experiments hold promise for future work involving the entanglement of two solitons and quantum information protocols based on topological states known as kinks.

6.1 Future work

These experiments offer a promising start for future work aimed at producing a soliton interferometer or developing quantum information protocols with solitons. Each direction offers specific rewards and presents particular technical challenges that need to be overcome. As stated above, a soliton interferometer could be revolutionary for cold atom sensor technology or precision measurement experiments due to the lack of wave-packet dispersion; however, this interferometer would by necessity operate in a low geometry configuration where the atom cloud is confined in two dimensions to prevent collapse. The result is that by gaining extremely long times for interrogation, one is forced to operate in a system that is more susceptible to vibration noise. This could be a poisoned pill that ultimately prevents such technology from maturing beyond the lab space. Nonetheless, the trade space for these experiments should be explored as certain guided atom-interferometry systems may be more robust than others, offering a net increase in precision or sensitivity.

Another open challenge is to demonstrate a coherent non-linear atom beam splitter

for solitons. Multiple protocols have been proposed by numerous theoretical investigations [66, 80, 81], but so far experimental demonstration has remained elusive. We believe this bottleneck is more due to the lack of an efficient and well controlled soliton production method, and fully expect significant progress to be made soon. Schemes simpler than those proposed above are also possible for proof of principle demonstrations. The experiments outlined in chapter 4 of this thesis represent a great starting point for these experiments. One could simply shine a tightly focused beam of resonant light into the center of the expanded center-of-mass wave function, punching a hole in the middle of it. The two remaining pieces would be coherent and split portions of the soliton wave function, and would interfere upon recombination. However, this method does not lend it self to tunable phase imprinting during the splitting operation, something that would be attractive for a soliton interferometer. A more sophisticated alteration to the experiments in chapter 4 would be to excite the soliton wave function inside the optical trap from the first excited state of the harmonic potential. This would produce a node at the center of the wave function and once the optical trap is snapped off, this wave function would expand resulting in a spatially separated Schrödinger Cat state identical to the output of a beam splitter. The phase between the two halves of the soliton wave function would be determined by the phase of the excitation pulse used to raise the atoms from the ground to first excited state inside the optical trap. Once this scheme, or one functionally equivalent to it is implemented controlled soliton interferometry for measurement purposes will be possible.

Experiments in chapter 5 demonstrated efficient and robust production of two independent solitons with uncontrolled relative phase. The main task for future experiments will be to design and implement a method for controlling (and ideally tuning) the relative phase to some set value. This would be essential for a more quantitative study of two soliton collisions. With this added technique future experiments could measure, Josephson population transfer between solitons [33], as well as phase imprinting during soliton collisions. Additionally, these experiments could explore the predictions for critical velocity of colliding solitons leading to collapse and

soliton-soliton fusion in a precise way [62, 32]. A detailed understanding of these effects is essential for future campaigns set on using bright atomic solitons as quantum memories, or exploring the realization of certain topological quantum computation schemes with solitons [29].

Bibliography

- [1] T. W Hänsch and A. L. Schawlow. Cooling of gases by laser radiation. *Optics Communications*, 13(1):68 – 69, 1975.
- [2] E. L. Raab, M. Prentiss, Alex Cable, Steven Chu, and D. E. Pritchard. Trapping of neutral sodium atoms with radiation pressure. *Phys. Rev. Lett.*, 59:2631–2634, Dec 1987.
- [3] Harald F. Hess. Evaporative cooling of magnetically trapped and compressed spin-polarized hydrogen. *Phys. Rev. B*, 34:3476–3479, Sep 1986.
- [4] Naoto Masuhara, John M. Doyle, Jon C. Sandberg, Daniel Kleppner, Thomas J. Greytak, Harald F. Hess, and Greg P. Kochanski. Evaporative cooling of spin-polarized atomic hydrogen. *Phys. Rev. Lett.*, 61:935–938, Aug 1988.
- [5] M. H. Anderson, J. R. Ensher, M. R. Matthews, C. E. Wieman, and E. A. Cornell. Observation of bose-einstein condensation in a dilute atomic vapor. *Science*, 269(5221):198–201, 1995.
- [6] K. B. Davis, M. O. Mewes, M. R. Andrews, N. J. van Druten, D. S. Durfee, D. M. Kurn, and W. Ketterle. Bose-einstein condensation in a gas of sodium atoms. *Phys. Rev. Lett.*, 75:3969–3973, Nov 1995.
- [7] C. C. Bradley, C. A. Sackett, J. J. Tollett, and R. G. Hulet. Evidence of bose-einstein condensation in an atomic gas with attractive interactions. *Phys. Rev. Lett.*, 75:1687–1690, Aug 1995.

- [8] Satyendra Bose. Plancks Gesetz und Lichtquantenhypothese. *Z. Phys.*, 26(3):178, 1924.
- [9] A. Einstein. Quantentheorie des einatomigen idealen Gases. Zweite Abhandlung. *Sitzungber. Preuss. Akad. Wiss.*, 1925:3, January 1925.
- [10] W. Ketterle. Nobel lecture: When atoms behave as waves: Bose-einstein condensation and the atom laser. *Rev. Mod. Phys.*, 74:1131–1151, Nov 2002.
- [11] N. N. Bogoliubov. On the theory of superfluidity. *J. Phys.(USSR)*, 1947.
- [12] M. Greiner, O. Mandel, T. Esslinger, T.W. Hansch, and I. Bloch. Quantum phase transition from a superfluid to a mott insulator in a gas of ultracold atoms. *Nature*, 415(6867):0039–0045, 2002.
- [13] C. Gross, T. Zibold, E. Nicklas, J. Estave, and M.K. Oberthaler. Nonlinear atom interferometer surpasses classical precision limit. *nature*, 464:1165, April 2010.
- [14] B. P. Anderson, P. C. Haljan, C. A. Regal, D. L. Feder, L. A. Collins, C. W. Clark, and E. A. Cornell. Watching dark solitons decay into vortex rings in a bose-einstein condensate. *Phys. Rev. Lett.*, 86:2926–2929, Apr 2001.
- [15] Kevin E. Strecker, Guthrie Partridge, Andrew Truscott, and Randall Hulet. Formation and propagation of matter-wave soliton trains. *Nature*, 417:150, May 2002.
- [16] L. Khaykovich, F. Schreck, G. Ferrari, T. Bourdel, J. Cubizolles, L. D. Carr, Y. Castin, and C. Salomon. Formation of a matter-wave bright soliton. *Science*, 296(5571):1290–1293, 2002.
- [17] Simon L. Cornish, Sarah T. Thompson, and Carl E. Wieman. Formation of bright matter-wave solitons during the collapse of attractive bose-einstein condensates. *Phys. Rev. Lett.*, 96:170401, May 2006.
- [18] B. Eiermann, Th. Anker, M. Albiez, M. Taglieber, P. Treutlein, K.-P. Marzlin, and M. K. Oberthaler. Bright bose-einstein gap solitons of atoms with repulsive interaction. *Phys. Rev. Lett.*, 92:230401, Jun 2004.

- [19] Franco Dalfovo, Stefano Giorgini, Lev P. Pitaevskii, and Sandro Stringari. Theory of bose-einstein condensation in trapped gases. *Rev. Mod. Phys.*, 71:463–512, Apr 1999.
- [20] R. J. Dodd, Mark Edwards, C. J. Williams, C. W. Clark, M. J. Holland, P. A. Ruprecht, and K. Burnett. Role of attractive interactions on bose-einstein condensation. *Phys. Rev. A*, 54:661–664, Jul 1996.
- [21] C. A. Sackett, J. M. Gerton, M. Welling, and R. G. Hulet. Measurements of collective collapse in a bose-einstein condensate with attractive interactions. *Phys. Rev. Lett.*, 82:876–879, Feb 1999.
- [22] L. D. Carr and Y. Castin. Dynamics of a matter-wave bright soliton in an expulsive potential. *Phys. Rev. A*, 66(6):063602, December 2002.
- [23] D. J. Korteweg and G. de Vries. On the change of form of long waves advancing in a rectangular canal, and on a new type of long stationary waves. *Philosophical Magazine Series 5*, 39(240):422–443, 1895.
- [24] Govind Agrawal. Nonlinear fiber optics. *Springer Berlin / Heidelberg*, 542:195–211, 2000.
- [25] M. Holzmann and J. Audretsch. Shaping an ultracold atomic soliton in a travelling wave laser beam. *EPL (Europhysics Letters)*, 40(1):31, 1997.
- [26] Alexander D. Cronin, Jörg Schmiedmayer, and David E. Pritchard. Optics and interferometry with atoms and molecules. *Rev. Mod. Phys.*, 81:1051–1129, Jul 2009.
- [27] Jun’ichi Ieda, Takahiko Miyakawa, and Miki Wadati. Exact analysis of soliton dynamics in spinor bose-einstein condensates. *Phys. Rev. Lett.*, 93:194102, Nov 2004.
- [28] S. Marcovitch and B. Reznik. Entanglement of solitons in the frenkel-kontorova model. *Phys. Rev. A*, 78:052303, Nov 2008.

- [29] J. Dziarmaga, W. H. Zurek, and M. Zwolak. Non-local quantum superpositions of topological defects. *Nat Phys*, 8:49, Jan 2012.
- [30] Alexej I. Streltsov, Ofir E. Alon, and Lorenz S. Cederbaum. Swift loss of coherence of soliton trains in attractive bose-einstein condensates. *Phys. Rev. Lett.*, 106:240401, Jun 2011.
- [31] N G Parker, A M Martin, S L Cornish, and C S Adams. Collisions of bright solitary matter waves. *Journal of Physics B: Atomic, Molecular and Optical Physics*, 41(4):045303, 2008.
- [32] A. D. Martin, C. S. Adams, and S. A. Gardiner. Bright matter-wave soliton collisions in a harmonic trap: Regular and chaotic dynamics. *Phys. Rev. Lett.*, 98:020402, Jan 2007.
- [33] N.G. Parker, A.M. Martin, C.S. Adams, and S.L. Cornish. Bright solitary waves of trapped atomic bose einstein condensates. *Physica D: Nonlinear Phenomena*, 238(15):1456 – 1461, 2009. *|ce:title|Nonlinear Phenomena in Degenerate Quantum Gases|/ce:title|*.
- [34] T. P. Billam, S. L. Cornish, and S. A. Gardiner. Realizing bright-matter-wave-soliton collisions with controlled relative phase. *Phys. Rev. A*, 83:041602, Apr 2011.
- [35] O. Carnal and J. Mlynek. Young’s double-slit experiment with atoms: A simple atom interferometer. *Phys. Rev. Lett.*, 66:2689–2692, May 1991.
- [36] F. Riehle, Th. Kisters, A. Witte, J. Helmcke, and Ch. J. Bordé. Optical ramsey spectroscopy in a rotating frame: Sagnac effect in a matter-wave interferometer. *Phys. Rev. Lett.*, 67:177–180, Jul 1991.
- [37] Mark Kasevich and Steven Chu. Atomic interferometry using stimulated raman transitions. *Phys. Rev. Lett.*, 67:181–184, Jul 1991.

- [38] David W. Keith, Christopher R. Ekstrom, Quentin A. Turchette, and David E. Pritchard. An interferometer for atoms. *Phys. Rev. Lett.*, 66:2693–2696, May 1991.
- [39] O. Nairz, A. Markus, and A. Zeilinger. Quantum interference experiments with large molecules. *American Journal of Physics*, 71:319, 2003.
- [40] S. Gerlich, S. Eibenberger, M. Tomandl, S. Nimmrichter, K. Hornberger, P. J. Fagan, J. Taxen, M. Mayor, and M. Arndt. Quantum interference of large organic molecules. *Nat Commun*, 2:263, 2011.
- [41] S. Groblacher, J. B. Hertzberg, M. R. Vanner, G. D. Cole, S. Gigan, K. C. Schab, and M. Aspelmeyer. Demonstration of an ultracold micro-optomechanical oscillator in a cryogenic cavity. *Nat Phys*, 5:485, 2009.
- [42] J. D. Thompson, B. M. Zwickl, A. M. Jayich, F. Marquardt, S. M. Girvin, and J. G. E. Harris. Strong dispersive coupling of a high-finesse cavity to a micromechanical membrane. *Nat*, 452:72, 2008.
- [43] A. Schliesser, R. Riviere, G. Anetsberger, O. Arcizet, and T. J. Kippenberg. Resolved-sideband cooling of a micromechanical oscillator. *Nat Phys*, 4:415, 2008.
- [44] William Marshall, Christoph Simon, Roger Penrose, and Dik Bouwmeester. Towards quantum superpositions of a mirror. *Phys. Rev. Lett.*, 91:130401, Sep 2003.
- [45] Oriol Romero-Isart, Mathieu L Juan, Romain Quidant, and J Ignacio Cirac. Toward quantum superposition of living organisms. *New Journal of Physics*, 12(3):033015, 2010.
- [46] M. Liu. *Quantum degeneracy in an attractive Bosonic system*. PhD thesis, Stanford University, 2007.

- [47] Wolfgang Ketterle, Kendall B. Davis, Michael A. Joffe, Alex Martin, and David E. Pritchard. High densities of cold atoms in a dark spontaneous-force optical trap. *Phys. Rev. Lett.*, 70:2253–2256, Apr 1993.
- [48] Ruquan Wang, Mingchang Liu, Francesco Minardi, and Mark Kasevich. Reaching ${}^7\text{Li}$ quantum degeneracy with a minitrap. *Phys. Rev. A*, 75:013610, January 2007.
- [49] J. Walls, R. Ashby, JJ Clarke, B. Lu, and WA Van Wijngaarden. Measurement of isotope shifts, fine and hyperfine structure splittings of the lithium D lines. *Eur. Phys. J. D*, 22(2):159–162, 2003.
- [50] N. C. Cizek. *Interplay of Attractive Interactions and Trap Anisotropy in Bose-Einstein Condensates*. PhD thesis, Stanford University, 2010.
- [51] E. R. I. Abraham, W. I. McAlexander, C. A. Sackett, and Randall G. Hulet. Spectroscopic determination of the s -wave scattering length of lithium. *Phys. Rev. Lett.*, 74(8):1315–1318, Feb 1995.
- [52] Wolfgang Ketterle and N. J. van Druten. Bose-einstein condensation of a finite number of particles trapped in one or three dimensions. *Phys. Rev. A*, 54:656–660, Jul 1996.
- [53] N. J. van Druten and Wolfgang Ketterle. Two-step condensation of the ideal bose gas in highly anisotropic traps. *Phys. Rev. Lett.*, 79:549–552, Jul 1997.
- [54] L. D. Carr and Y. Castin. Dynamics of a matter-wave bright soliton in an expulsive potential. *Phys. Rev. A*, 66(6):063602, December 2002.
- [55] Y. Castin and C. Herzog. Bose–Einstein condensates in symmetry breaking states. *C. R. Hebd. Seances Acad. Sci., Ser. A B, Sci. Math. Sci. Phys.*, 2(3):419–443, 2001.
- [56] E.J. Mueller, T.L. Ho, M. Ueda, and G. Baym. Fragmentation of Bose-Einstein condensates. *Phys. Rev. A*, 74(3):33612, 2006.

- [57] V.A. Yurovsky, M. Olshanii, and D.S. Weiss. Collisions, correlations, and integrability in atom waveguides. *Adv. At. Mol. Opt Phys*, 55:61–138, 2008.
- [58] Subhasis Sinha, Alexander Yu. Cherny, Dmitry Kovrizhin, and Joachim Brand. Friction and diffusion of matter-wave bright solitons. *Phys. Rev. Lett.*, 96:030406, Jan 2006.
- [59] H. Buljan, M. Segev, and A. Vardi. Incoherent matter-wave solitons and pairing instability in an attractively interacting bose-einstein condensate. *Phys. Rev. Lett.*, 95(18):180401, Oct 2005.
- [60] A. I. Streltsov, O. E. Alon, and L. S. Cederbaum. Formation and dynamics of many-boson fragmented states in one-dimensional attractive ultracold gases. *Phys. Rev. Lett.*, 100:130401, April 2008.
- [61] Ø. Elgarøy and C. J. Pethick. Absence of fragmentation of the condensate in a model for bosons in a trap. *Phys. Rev. A*, 59:1687, February 1999.
- [62] L. Salasnich, A. Parola, and L. Reatto. Condensate bright solitons under transverse confinement. *Phys. Rev. A*, 66:043603, Oct 2002.
- [63] Lorenz S. Cederbaum, Alexej I. Streltsov, and Ofir E. Alon. Fragmented metastable states exist in an attractive Bose-Einstein condensate for atom numbers well above the critical number of the Gross-Pitaevskii theory. *Phys. Rev. Lett.*, 100:040402, January 2008.
- [64] T. P. Billam, S. A. Wrathmall, and S. A. Gardiner. Variational determination of approximate bright matter-wave soliton solutions in anisotropic traps. *Phys. Rev. A*, 85:013627, Jan 2012.
- [65] Y. Castin. Internal structure of a quantum soliton and classical excitations due to trap opening. *The European Physical Journal B - Condensed Matter and Complex Systems*, 68:317–328, 2009. 10.1140/epjb/e2008-00407-3.
- [66] Christoph Weiss and Yvan Castin. Creation and detection of a mesoscopic gas in a nonlocal quantum superposition. *Phys. Rev. Lett.*, 102:010403, Jan 2009.

- [67] P. Medley, M. A. Minar, D. Berryrieser, and M. A. Kasevich. Evaporative production of bright atomic solitons. *Arxiv*, 0, Feb 2012.
- [68] M. Wadati. Soliton propagations in the electromagnetically induced transparency. *The European Physical Journal - Special Topics*, 173:223–232, 2009. 10.1140/epjst/e2009-01075-9.
- [69] Lev Khaykovich and Boris A. Malomed. Deviation from one dimensionality in stationary properties and collisional dynamics of matter-wave solitons. *Phys. Rev. A*, 74:023607, Aug 2006.
- [70] Alexej I. Streltsov, Ofir E. Alon, and Lorenz S. Cederbaum. Swift loss of coherence of soliton trains in attractive bose-einstein condensates. *Phys. Rev. Lett.*, 106:240401, Jun 2011.
- [71] U. Al Khawaja, H. T. C. Stoof, R. G. Hulet, K. E. Strecker, and G. B. Partridge. Bright soliton trains of trapped bose-einstein condensates. *Phys. Rev. Lett.*, 89:200404, Oct 2002.
- [72] A. D. Martin, C. S. Adams, and S. A. Gardiner. Bright solitary-matter-wave collisions in a harmonic trap: Regimes of solitonlike behavior. *Phys. Rev. A*, 77:013620, Jan 2008.
- [73] Thawatchai Mayteevarunyoo, Boris A. Malomed, and Monai Krairiksh. Stability limits for two-dimensional matter-wave solitons in a time-modulated quasi-one-dimensional optical lattice. *Phys. Rev. A*, 76:053612, Nov 2007.
- [74] J. P. Gordon. Interaction forces among solitons in optical fibers. *Opt. Lett.*, 8:596–598, 1983.
- [75] George I. Stegeman and Mordechai Segev. Optical spatial solitons and their interactions: Universality and diversity. *Science*, 286(5444):1518–1523, 1999.
- [76] M. A. Minar, P. Medley, D. Berryrieser, and M. A. Kasevich. Much ado about solitons. *Arxiv*, 0, Feb 2012.

- [77] U Al Khawaja and H T C Stoof. Formation of matter-wave soliton molecules. *New Journal of Physics*, 13(8):085003, 2011.
- [78] Maciej Lewenstein and Boris A Malomed. Entanglement generation by collisions of quantum solitons in the born approximation. *New Journal of Physics*, 11(11):113014, 2009.
- [79] B J Dabrowska-Wüster, S Wüster, and M J Davis. Dynamical formation and interaction of bright solitary waves and solitons in the collapse of bose-einstein condensates with attractive interactions. *New Journal of Physics*, 11(5):053017, 2009.
- [80] A. D. Martin and J. Ruostekoski. Quantum dynamics of atomic bright solitons under splitting and re-collision, and implications for interferometry. *arxiv/cond-mat*, 1111.5686, 2011.
- [81] Alexej I. Streltsov, Ofir E. Alon, and Lorenz S. Cederbaum. Scattering of an attractive bose-einstein condensate from a barrier: Formation of quantum superposition states. *Phys. Rev. A*, 80:043616, Oct 2009.